



Contents lists available at ScienceDirect

## Ore Geology Reviews

journal homepage: [www.elsevier.com/locate/oregeorev](http://www.elsevier.com/locate/oregeorev)

# Trace-element compositions of sulfides from inactive Tianzuo hydrothermal field, Southwest Indian Ridge: Implications for ultramafic rocks hosting mineralization

Teng Ding <sup>a,b,c</sup>, Jia Wang <sup>a</sup>, Chunhui Tao <sup>a,c,d,\*</sup>, Ágata Alveirinho Dias <sup>e,f</sup>, Jin Liang <sup>c</sup>, Yuan Wang <sup>a,c</sup>, Jie Chen <sup>c</sup>, Bin Wu <sup>g</sup>, Hui Huang <sup>g</sup>

<sup>a</sup> Institute of Marine Geology, College of Oceanography, Hohai University, Nanjing 210098, China

<sup>b</sup> Key Laboratory of Metallogenetic Prediction of Nonferrous Metals and Geological Environment Monitoring (Central South University), Ministry of Education, Changsha 410083, China

<sup>c</sup> Key Laboratory of Submarine Geosciences, Second Institute of Oceanography, Ministry of Natural Resources, Hangzhou 310012, China

<sup>d</sup> School of Oceanography, Shanghai Jiaotong University, Shanghai 200030, China

<sup>e</sup> Institute of Science and Environment, University of Saint Joseph, Rua de Londres 106, Macao, China

<sup>f</sup> Instituto Dom Luiz, Faculty of Sciences of the University of Lisbon, Campo Grande, Ed. C1, Piso 1, Portugal

<sup>g</sup> State Key Laboratory of Nuclear Resources and Environment, East China University of Technology, Nanchang 330013, China

## ARTICLE INFO

## Keywords:

SWIR  
Tianzuo  
Sulfide  
Ultramafic rocks  
Trace-element  
Serpentinization

## ABSTRACT

The recently explored inactive Tianzuo hydrothermal field, in the amagmatic segment of the ultraslow-spreading Southwest Indian Ridge (SWIR), is closely associated with detachment faults. In this site, sulfide minerals are hosted by serpentine-bearing ultramafic rocks and include high-temperature (isocubanite, sphalerite, and minor pyrrhotite) and low-temperature (pyrite I, marcasite, pyrite II, and covellite) phases. In this study, trace-element concentrations of isocubanite and pyrite II were used to elucidate mineralization processes in ultramafic rocks hosting sulfides. Results show that isocubanite is enriched in metals such as Cu, Co, Sn, Te, Zn, Se, Pb, Bi, Cd, Ag, In, and Mn, and pyrite II is enriched in Mo and Tl. The marked enrichment in Te, Cu, Co, and In in isocubanite (compared with Se, Zn, Ni, and Sn, respectively) is most likely due to the contribution of magmatic fluids from gabbroic intrusions beneath the hydrothermal field. The intrusion of gabbroic magmas would have enhanced serpentinization reactions and provided a relatively oxidizing environment through the dissolution of anhydrite precipitated previously in the reaction zone, within high temperature and low pH conditions. This might have facilitated the extraction of metals by initial hydrothermal fluids, leading to the general enrichment of most metals in isocubanite. Metals in pyrite II have compositions similar to those of isocubanite, except for strong depletion in magmatically derived Te, Cu, Co, and In. This means that serpentinization processes had a dominating role in pyrite II precipitation as well. The enrichment of pyrite II in Mo and Tl is also indicative of seawater contribution in its composition. The study concludes that serpentinization reactions contribute effectively both to high- and low-temperature sulfide mineralization at Tianzuo hydrothermal field, with gabbroic intrusions further promoting high-temperature sulfide mineralization, providing additional metals, fluids and heat. In contrast, low-temperature sulfide mineralization occurred during the cooling of gabbroic intrusions, with decreasing rates of serpentinization reactions and a significant influence of seawater.

## 1. Introduction

Due to the close association between basalts and hydrothermal activity, it is commonly considered that basaltic eruptions dominate hydrothermal circulation along sediment-starved oceanic ridges, which

may extract ore-forming materials from wall rocks before their precipitation as sulfides on the seafloor (e.g., Large, 1992; Shanks, 2001; Hannington et al., 2005; Seal, 2006; Keith et al., 2016; Grant, et al., 2018). This results in most sulfide deposits being hosted in basalts, especially at fast-spreading ridges (Baker et al., 1996). The ultraslow-

\* Corresponding author.

E-mail address: [taochunhuimail@163.com](mailto:taochunhuimail@163.com) (C. Tao).

<https://doi.org/10.1016/j.oregeorev.2021.104421>

Received 24 July 2020; Received in revised form 11 June 2021; Accepted 17 August 2021

Available online 23 August 2021

0169-1368/© 2021 Elsevier B.V. All rights reserved.

spreading ridges were considered to lack hydrothermal fields because of the scarce magmatic activity (Baker et al., 1996). However, further studies proved that axial sulfide deposits can develop in such ridges, such as Mt. Jourdanne in Southwest Indian Ridge (SWIR; Münch et al., 2001), Loki's Castle along Arctic Mid-Ocean Ridge (AMOR; Pedersen et al., 2010), and Piccard along Mid-Cayman Rise (Kinsey and German, 2013). At the ultraslow-spreading SWIR, the first observed active black-smoker chimney at Longqi (49.6°E; Tao et al., 2012), ended the controversy concerning whether sulfide deposits can develop in such ridges. Subsequently, several more hydrothermal fields have been discovered near the Longqi field, including the Yuhuang (49.3°E), Xilongjing (49.7°E), Duanqiao (50.4°E), Changbai (~51.0°E), and Zhanqiao (~51.0°E) fields (Tao et al., 2014; Yang et al., 2017b; Liao et al., 2018; Yuan et al., 2018). A significant feature of ultraslow-spreading ridges is that they can be divided into magmatic and amagmatic segments based on their association with magmatism, as in the case of the SWIR (Sauter et al., 2009; Standish and Sims, 2010). The extensive occurrence of basalts in hydrothermal fields along these ultraslow-spreading ridges suggests a close association of these fields with magmatic activity as well.

In addition to axial hydrothermal systems associated with basaltic activities, the hydrothermal fields closely related to ultramafic rocks have been recognized as another type of hydrothermal system, which mainly developed along slow- and ultraslow-spreading ridges (e.g., Hannington et al., 2005). The first sulfide ultramafic-hosted hydrothermal vent field, Logatchev, was discovered along the MAR (Krasnov et al., 1995). After that, other sulfide and non-sulfide ultramafic-hosted fields were identified along slow- and ultraslow-spreading ridges, such as Rainbow (German et al., 1996), Lost City (Kelley et al., 2001), Ashadze (Beltenev et al., 2002), Menez Hom (Fouquet et al., 2002), Saldanha (Dias and Barriga, 2006), Semyonov (Beltenev et al., 2007), and Nibelungen (Melchert et al., 2008) along MAR, Von Damm from Mid-Cayman Rise (Connelly et al., 2012), Kairei from CIR (Wang, 2012), and Tianzuo from SWIR (Tao et al., 2014). Unlike their counterparts hosted in basalts, studies for ultramafic-hosted sulfide deposits are quite few, leading to the mineralization processes still unclear. Nevertheless, for on-land ultramafic-hosted sulfide deposits, if not clearly of magmatic origin, are thought to be linked to serpentinization processes involving the remobilization of metals from primary silicate minerals (e.g., olivine) into hydrothermal sulfides (if sufficient H<sub>2</sub>S is available) (e.g., Outokumpus of Finland, Gaál and Parkkinen, 1993; Loukola-Ruskeeniemi, 1999, and Kidd Creek of Canada, Barrie et al., 1999).

However, a growing number of studies have implied that even in hydrothermal fields hosted in tectonic-related hydrothermal systems, fluids may circulate through mafic basalts. For example, the analysis of vent fluids in active seafloor hydrothermal systems has shown that concentrations of most elements (e.g. Mn, Zn, Cu, Ag, Ba, Cd, Rb and As) are comparable in hydrothermal systems associated with ultramafic and basaltic rocks (Jean-Baptiste et al., 1991; Wetzel and Shock, 2000; Charlou et al., 1998, 2002; Douville et al., 2002; Schmidt et al., 2007). In addition, the MAR Logatchev-2 and Rainbow hydrothermal fields have a Cu-Zn mineralization contrasting with the distinct Cu mineralization of the Logatchev-1 field, even though these fields are restricted to serpentinite protrusions, meaning that the primary ultramafic rocks did not control the metallogeny of ores associated with them (Lein et al., 2001). Moreover, Allen and Seyfried (2004) further proposed that even for the Lost City system, which was dominated by low-temperature carbonate precipitates, serpentinization likely played an insignificant role accounting for hydrothermal circulation compared with hot lithospheric units and/or near magmatic heat sources, as the chemical compositions of vent fluids from this hydrothermal field are virtually unchanged from the seawater values. These mean that the sulfide mineralization mechanisms associated with ultramafic rocks are still obscure, an improved understanding of sulfide mineralization along oceanic ridges thus requires the elucidation of sulfide mineralization hosted in ultramafic rocks.

The recently discovered Tianzuo hydrothermal field (27°57'S, 63°32'E) in the easternmost ultraslow-spreading SWIR is an inactive sulfide hydrothermal field hosted in ultramafic rocks associated with detachment faults (Tao et al., 2014; Cao et al., 2018; Chen et al., 2018). Based on the previously mineralogical observation (Cao et al. 2018), the sulfide assemblage was further studied in this research, and we found that the sulfide minerals from this field can be subdivided into high-temperature (isocubanite, sphalerite, and minor pyrrhotite) and low-temperature (pyrite I, marcasite, pyrite II, and covellite) assemblages. This means that these sulfide minerals can be the indicators showing the sources and evolution for the ore-forming hydrothermal fluids where they precipitated. Consequently, our study aimed to use major- and trace-element compositions of isocubanite and pyrite II from the Tianzuo hydrothermal field as indicators in explaining sulfide mineralization hosted by ultramafic rocks, and to improve our understanding of sulfide mineralization in the SWIR and other slow- and ultraslow-spreading oceanic ridges.

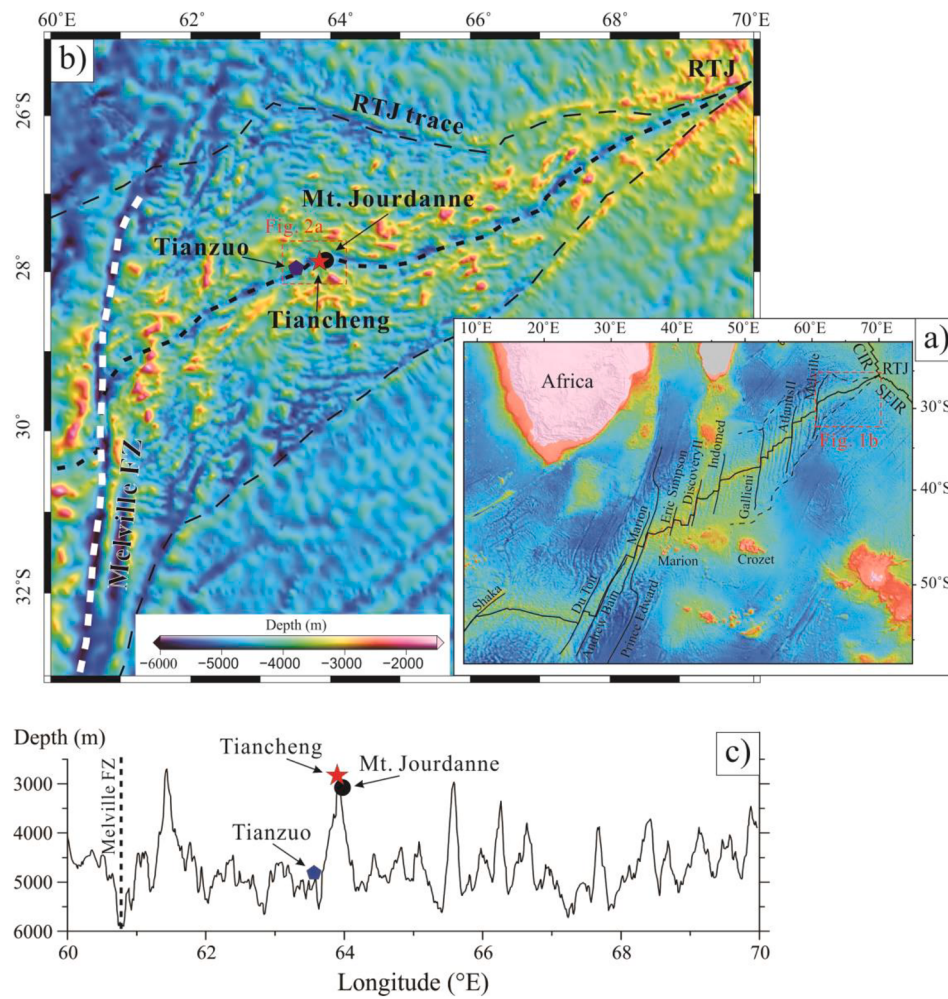
## 2. Geological setting

### 2.1. Geology of SWIR

The SWIR separates the African and Antarctic plates, from the Bouvet Triple Junction (BTJ; 0°E) in the west to the Rodrigues Triple Junction (RTJ; 70°E) in the east (Fig. 1a). This ridge extends for ~8000 km with an almost constant spreading rate of ~14 mm yr<sup>-1</sup> and it is one of the slowest-spreading ridges globally (Dick et al., 2003; Horner-Johnson et al., 2005). The ridge is characterized by very rugged submarine topography with an axial rift valley and water depths of >5000 m. The SWIR is cut by a series of N-S-striking transform faults that divide it into individual segments with distinct geological characteristics (Cannat et al., 1999). Bathymetric data reveal a shallow central region between the Prince Edward (35°E) and Gallieni (52°20' E) fracture zones, with an average depth of ~3200 m (Fig. 1a; Sauter et al., 2001; Cannat et al., 2008). This bathymetric high land is correlated with negative residual mantle Bouguer gravity anomalies and was expressed as thick oceanic crust, indicating a robust magma supply since 10–8 Ma, probably associated with the Crozet and Marion hotspots (Sauter et al., 2004, 2009; Zhang et al., 2013; Zhou and Dick, 2013; Yang et al., 2017a). This area also hosts most of the hydrothermal activities discovered to date. Unlike the region between the Prince Edward and Gallieni fracture zones, the easternmost SWIR region between the Melville Fracture Zone (61°E) and RTJ has no transform faults (Fig. 1b), with a smooth seafloor between two ridge flanks (Cannat et al., 2003; Sauter et al., 2013). This indicates an anomalously low average melt supply and strong tectonism. There has been no obvious magmatic activity for at least 26 Myr in this region (Cannat et al., 2006). Compared with other segments of the ridge, the easternmost SWIR has the greatest water depth (4730 m) and thinnest (or missing) crust, with these features being attributed to lower mantle temperatures and lower degrees of mantle melting (Minshull et al., 2006; Cannat et al., 2008). However, several segments with robust magma supply and high relief (e.g., at ~61.5°E, 64°E, and 65.5°E) exist along the easternmost SWIR (Fig. 1c), displaying volcanic structures several tens of meters high, with lateral extension for several tens of kilometers.

### 2.2. Geology of the Tianzuo hydrothermal field

The Tianzuo hydrothermal field was discovered during the COMRA DY115-20 cruise of the R/V *Da Yang Yi Hao* in 2009 (Tao et al., 2014), and lies in Segment 11 of the SWIR, near the inactive Mt Jourdanne and active Tiancheng fields (Fig. 2a; Münch et al., 2001; Nayak et al., 2014; Cao et al., 2018; Chen et al., 2018). Further detailed investigations of this hydrothermal site were carried out by the Chinese manned submersible *Jiaolong* during the COMRA DY115-35 cruise of the R/V *Xiang Yang Hong 9* in 2014–2015. Segment 11 has an hourglass shape



1

**Fig 1.** (a) Geotectonic setting and topography of the Southwest Indian Ridge (Modified from Chen et al., 2018); (b) the area between the Melville fracture zone and the Rodrigues Triple Junction (Modified from Chen et al., 2018). Ridge segments and non-transform faults are based on Cannat et al. (1999) and Sauter et al. (2001); (c) along-axis bathymetric profile between 60°E and 70°E (modified from Cannat et al., 2003).

extending N–S for >20 km, with an axial volcanic ridge bounded to the east and west by a non-transform discontinuity (NTD; Fig. 2a). Along-axis topography in Segment 11 varies within ~2700 m, and crustal thickness is >6 km at the center with high relief, with an average thickness of ~4 km. Maximum crustal thicknesses in adjacent low-relief segments are 2–3 km, indicating focused and variable magmatic accretion (Fig. 2b; Cannat et al., 1999, Cannat et al., 2003). Segment 11 may be dominated by strong melt-focusing processes, similar to other segments along the SWIR such as those between the Prince Edward and Gallieni fracture zones (Cannat et al., 1999; Sauter et al., 2001; Sato et al., 2013). The inactive Mt Jourdanne and adjacent active Tancheng (with low-temperature diffuse flows) hydrothermal fields are located in a volcanic structure along the rift axis, at water depths of 2750 and 2950 m, respectively (Fig. 2a and c). Outcrops in both of these fields comprise predominantly basaltic rocks (Münch et al., 2001; Tao et al., 2014; Chen et al., 2018).

The Tianzuo hydrothermal field, located ~14 km southeast of the Tianzuo Seamount at a water depth of 3630 m, was the first confirmed ultramafic-hosted hydrothermal field at the SWIR. It is situated on top of a dome-shaped structure typically associated with oceanic detachment faults (Fig. 2d; Standish and Sims, 2010), and ultramafic outcrops, distinct from adjacent fields (Fig. 2a–d). Hydrothermal activity is likely controlled by the detachment fault, as in the Logatchev and Rainbow fields (German et al., 1996; Schmidt et al., 2007). The DY115-20 cruise

and 88th *Jiaolong* dive found that the main outcrops of the Tianzuo field are altered ultramafic rocks and hydrothermal precipitates with no significant evidence of magmatic activity or typical vent fauna (Fig. 3), indicating that hydrothermal activity is ancient. Adjacent areas near the Tianzuo hydrothermal field are covered by gray sediments (Fig. 3a and c), distinct from the Tianzuo field itself where red-brown sediments occur over an area of about 800 m × 530 m (Fig. 3b and d). Strongly weathered opal and massive sulfides are exposed on the seafloor in the Tianzuo hydrothermal field (Fig. 3b and d). Samples analyzed in the present study were collected from the seafloor during the 88th *Jiaolong* dive and include mostly sulfides and serpentinized peridotites (Fig. 3e–f). Representative samples of each type were collected by submersible *Jiaolong* when we travelled through this field westwards, including four fresh serpentinized ultramafic rocks collected from the marginal area of this field and three relative fresh sulfide samples collected from the sulfide mound (Fig. 3e–f).

### 2.3. Petrography and mineralogy

#### 2.3.1. Mineralogy of serpentinized ultramafic rocks

Serpentinized ultramafic rocks collected from the Tianzuo hydrothermal field generally contain large light-colored pyroxene phenocrysts surrounded by black serpentine minerals (Fig. 3e). Microscopic textures indicate that the samples contain abundant crystal relicts, including

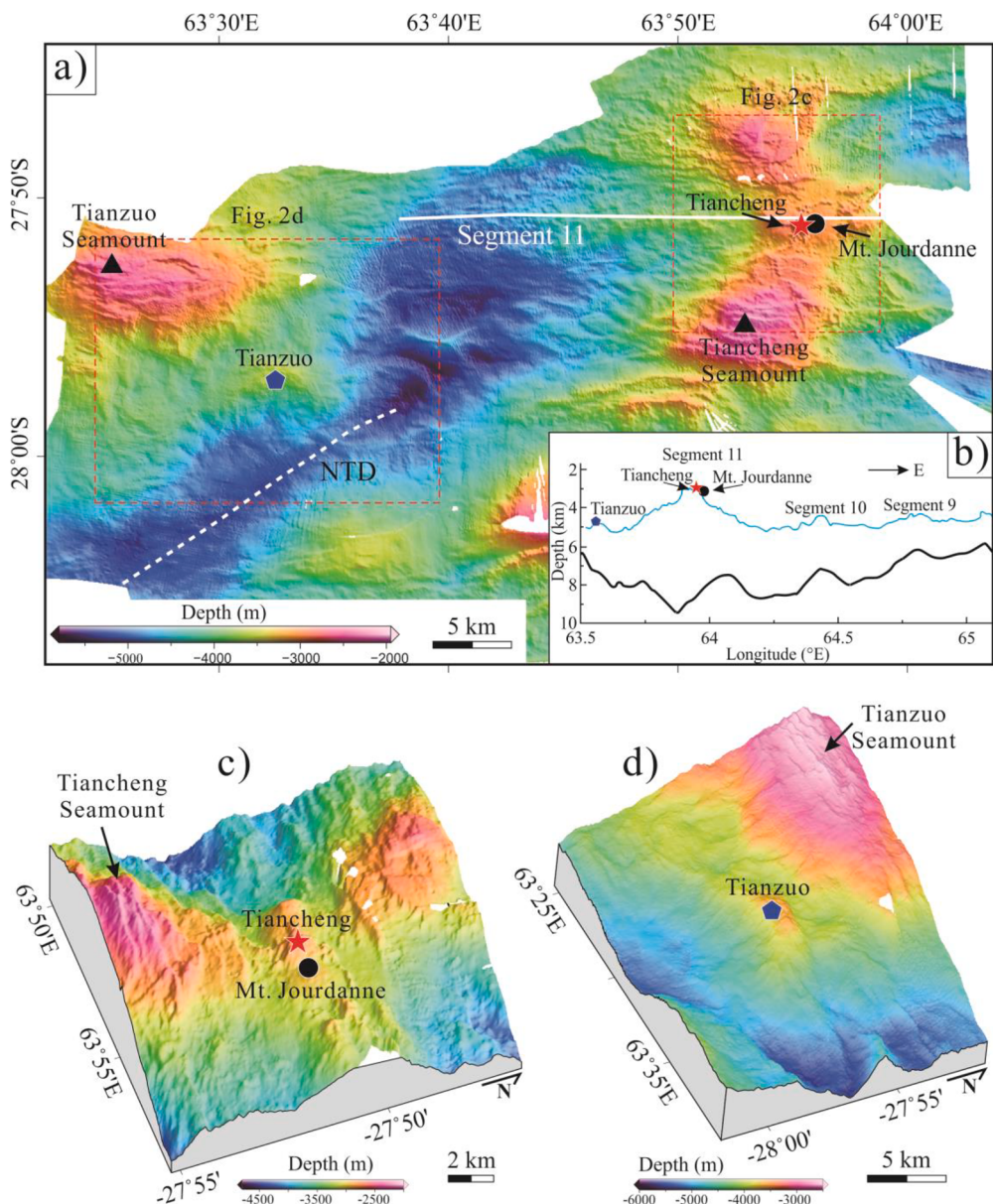


**Fig. 2.** (a) Topography of the Tiansuo hydrothermal field and the adjacent Tiancheng and Mt Jourdanne fields (Modified from Chen et al., 2018); (b) along-axis topography and Moho depth of segments #9, #10, and #11 (modified from Cannat et al., 2003). Blue and thick black lines indicate topography and Moho depth as predicted from gravity, respectively; (c, d) three-dimensional views around the Tiancheng and Mt. Jourdanne (c) and Tiansuo (d) hydrothermal fields (Modified from Chen et al., 2018).

pyroxene, olivine, and minor spinel (Fig. 4a–d). Pyroxene is dominated by clinopyroxene, usually with altered rims and crosscut by magnetite and chrysotile veinlets (Fig. 4a–b), indicating that the source rocks of serpentinized ultramafic rocks were most likely wehrlite. Pyroxene bastites also display jagged “tears” on the surface, indicating an extensional environment (Fig. 4b). Olivine is usually surrounded by a network of serpentine veinlets and cut by magnetite veinlets that display pseudomorphous mesh and hourglass textures after olivine (Fig. 4c and e). Spinels are usually surrounded or cut by serpentine minerals and replaced by magnetite (Fig. 4d). The lizardite and chrysotile can be identified in thin sections, generally replacing clinopyroxene, olivine, and spinel, and displaying pseudomorphous textures after these minerals (Fig. 4). In addition to the abundant magnetite veinlets that crosscut serpentine minerals (Fig. 4a, c), many subhedral to euhedral magnetite grains occur with a pseudomorphous texture after olivine (Fig. 4e–h). Contemporary hematite is observed coexisting with subhedral to euhedral magnetite grains (Fig. 4f–h), probably indicating a relatively oxidizing environment during serpentinization reactions. Minor quartz veinlets also occur within the serpentine minerals, possibly a product of serpentinization.

### 2.3.2. Mineralogy and paragenesis of sulfides

Sulfides observed in the sulfide mound are mostly yellow-brown in color, since they are covered by red iron oxide as a result of weathering (Fig. 3f). Sulfide minerals, including major pyrite and isocubanite and minor pyrrhotite, sphalerite, and covellite, constitute >70% of the ore, and are present as anhedral grains with rare subhedral to euhedral crystals disseminated in serpentine-bearing ultramafic rocks (Figs. 5–6). Serpentine and quartz constitute the other 30% of the ore, occurred as brown or red color with abundant holes, most likely resulting from strong weathering.

Pyrite is the most abundant sulfide phase and it is either hosted in serpentine minerals or coexists with quartz (Figs. 5 and 6; Cao et al., 2018). Based on its morphology, pyrite can be subdivided into two types, pyrite I and II. Pyrite I generally coexisted with marcasite occurring as colloform texture and pseudomorphically replace pyrrhotite plates (Figs. 5 and 6). Pyrite II generally occurred as the results of replacement for pyrite I with the retention of marcasite relicts (Fig. 6a), sometimes, pyrite I was absent because of the complete replacement, or due to the erosion of strong weathering, resulting abundant holes surrounded by pyrite II rims (Fig. 5a, c, f). Pyrite II crystals also typically

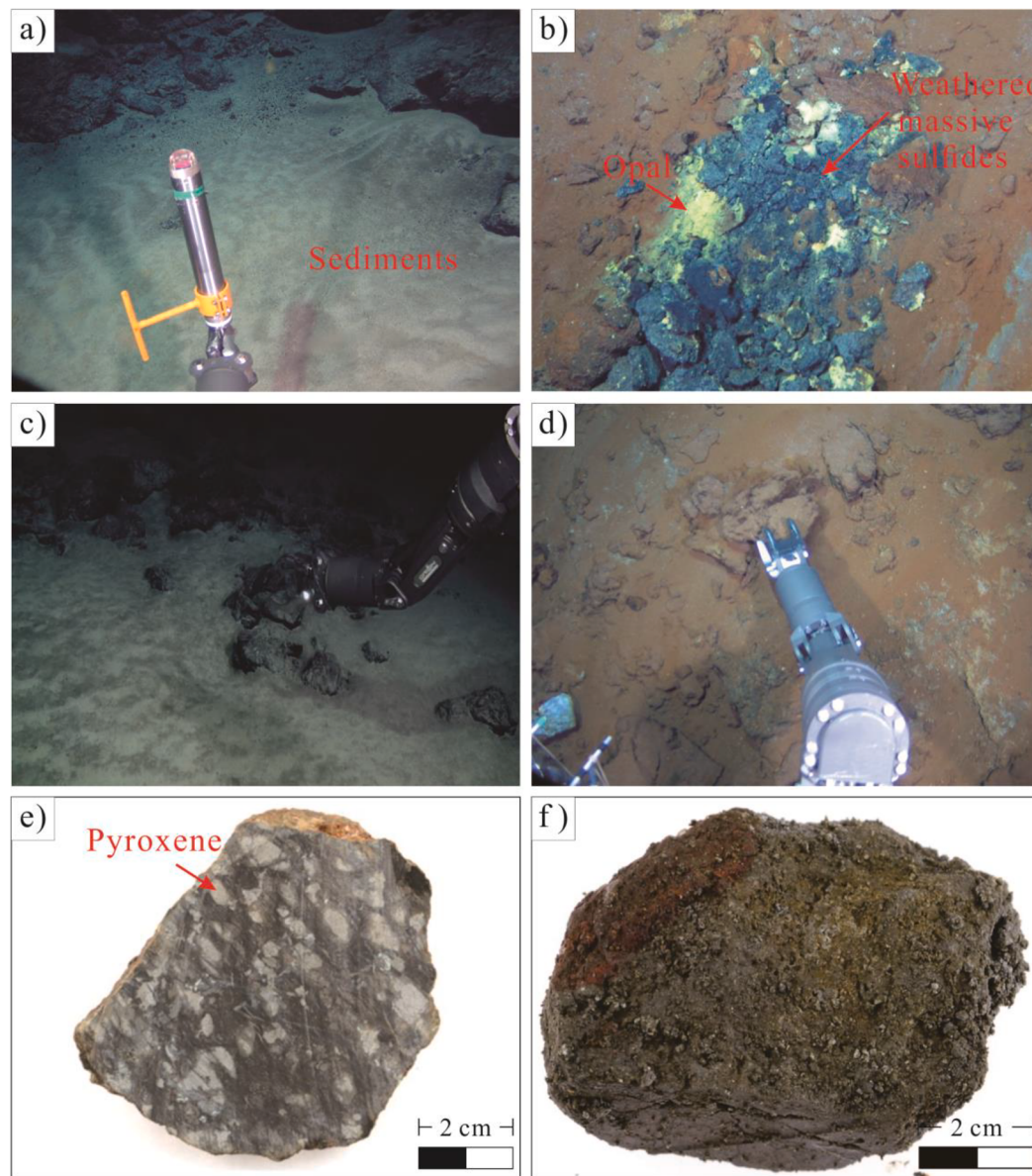


**Fig. 3.** (a) Gray sediments covering the adjacent area near the Tiansuo hydrothermal field, and (b) red-brown sediments in the Tiansuo hydrothermal field. Weathered massive sulfides and opal are commonly observed on the seafloor; (c, d) photographs showing the manned submersible *Jiaolong* obtaining samples from the Tiansuo hydrothermal field and the adjacent area; (e, f) representative photographs of samples obtained from the Tiansuo hydrothermal field: (e) the altered ultramafic rock sample with pyroxene phenocrysts surrounded by serpentine minerals, and (f) sulfide sample covered by red iron oxide collected from the sulfide mound. Fig. 3b, e, f are quoted from Ding et al. (2021).

grow around and replace early isocubanite and sphalerite, or occur as individual grains in quartz veinlets with no inclusions visible under microscopic examination (Figs. 5 and 6). Marcasite is unstable and can only precipitate at relatively low temperatures ( $<200^{\circ}\text{C}$ ) and low pH ( $<4.5$ ), undergoing transformation to pyrite at temperatures of  $>350^{\circ}\text{C}$  (Fleet, 1970; Koski et al., 1984; Graham et al., 1988). This suggests that pyrite in Tiansuo hydrothermal field precipitated later and crystallized during a low-temperature phase; this is particularly the case for pyrite II, which also replaces pyrite I.

Isocubanite disseminated in serpentine minerals is easy to be distinguished from other sulfide minerals in the Tiansuo field (Fig. 5). Isocubanite displays an anhedral shape and brown color, usually with grid structures typically resulting from exsolution from other Cu–Fe sulfides such as chalcopyrite, with this being further indicated by its Cu-rich rims as illustrated in Fig. 5c. There are no obvious crosscutting relationships between isocubanite, sphalerite, and pyrrhotite (or pyrite I with pseudomorphic texture after pyrrhotite), so precipitation of isocubanite was likely contemporaneous with crystallization of pyrrhotite and sphalerite (Fig. 5). Isocubanite displays obvious replacement by late pyrite II (Fig. 5b, d and 6c), so its precipitation must pre-date that of

pyrite II. Experimental studies of phase relationships of reactions in Cu–Fe–S and Fe–S systems indicate that at temperatures of  $>335^{\circ}\text{C}$ , isocubanite begins to crystallize with chalcopyrite, pyrite, and pyrrhotite (Lusk and Bray, 2002). Isocubanite was thus likely precipitated during the high-temperature phase of the Tiansuo hydrothermal system.

Pyrrhotite is rare in Tiansuo sulfide samples; it is usually included in pyrite II with an anhedral shape and as a relict replaced by late pyrite II (Fig. 5f). This indicates that the sulfide ores in Tiansuo field were originally enriched in pyrrhotite, which was almost completely replaced by pyrite, resulting in few pyrrhotite relicts in pyrite II (Fig. 5f), and abundant pseudomorphic textures (Fig. 6b and e).

Sphalerite is also rare in sulfides collected from the Tiansuo hydrothermal field. It is generally anhedral, gray in color, and contains abundant isocubanite or, conversely, is included in isocubanite as exsolution lamellae (Fig. 5d–e), indicating that the precipitation of sphalerite was contemporaneous with that of isocubanite during early high-temperature mineralization.

Covellite is blue in color and usually replaces sphalerite with an anhedral morphology (Fig. 5d–e), or occurs in quartz veinlets as lamellae or fibrous aggregates (Fig. 6f). An atomic Cu:S ratio of 1:1 was

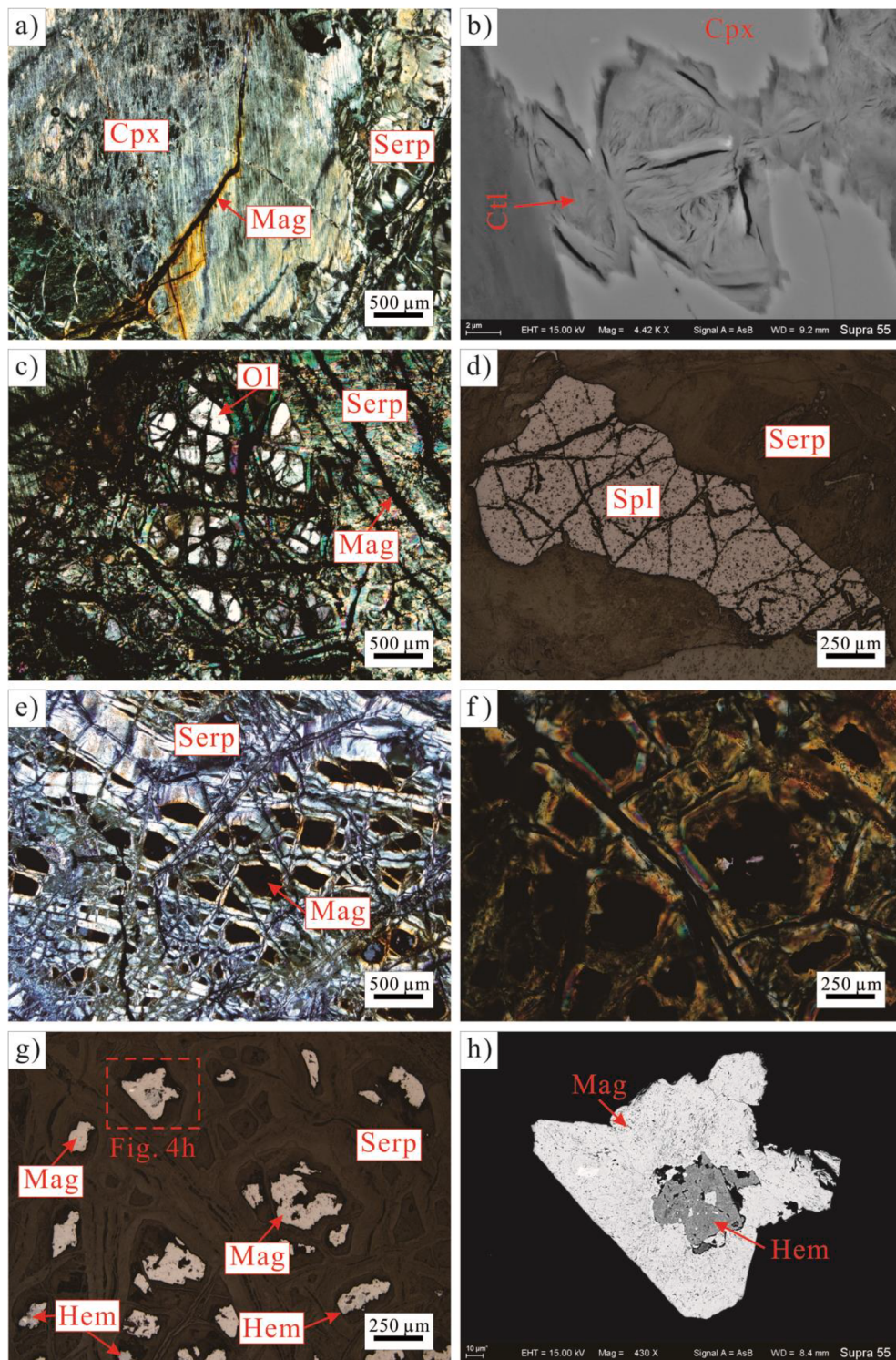


**Fig. 4.** Photomicrographs showing representative textures and minerals observed of ultramafic rocks samples from the Tianzuo hydrothermal field: (a) partially serpentized peridotite showing clinopyroxene phenocrysts surrounded by serpentinite minerals, both of which are crosscut by late magnetite veinlets (cross-polarized light); (b) clinopyroxene altered to chrysotile showing jagged “tears” on the surface (back-scattered electron (BSE) image); (c) mesh texture where is observed relict unaltered olivine in the center surrounded by a network of serpentinite veinlets between olivine grains and cut by magnetite (cross-polarized light); (d) relicts of fractured spinel grains in serpentinite matrix (reflected light); (e) ultramafic rocks altered to serpentinite minerals with a mesh texture consisting of magnetite grains surrounded by a network of serpentinite veinlets (cross-polarized light); (f-h) Magnetite coexisting with hematite in serpentized-ultramafic samples (f: cross-polarized light, g: reflected light, and h: BSE image). Abbreviations: Mag: magnetite; Serp: serpentinite; Cpx: clinopyroxene; Ctl: chrysotile; Ol: Olivine; Spl: spinel; Hem: hematite.

obtained by EMPA (Cao et al., 2018). Covellite is a low-temperature sulfide phase generally found in massive sulfide samples (Lusk and Bray, 2002). Both pyrite II and covellite occur in quartz veinlets, probably indicating their contemporaneous precipitation during late-stage low-temperature mineralization.

On the basis of these observations, we conclude that sulfide mineralization in the Tianzuo hydrothermal field occurred in two stages: an early high-temperature stage ( $>335$  °C; including isocubanite, sphalerite, and pyrrhotite), and a late low-temperature stage ( $<200$  °C; including pyrite, marcasite, and covellite), as illustrated in Fig. 7.

### 3. Analytical methods

#### 3.1. Preliminary mineralogy and SEM analyses

Serpentinized ultramafic rocks and massive sulfide samples from the Tianzuo hydrothermal field were prepared as thin-sections for analysis. Mineralogy and textural-structural relationships were investigated under transmitted and reflected light with a petrographic microscope. Scanning electron microscope (SEM) was conducted by using a Zeiss Supra 55 instrument at the State Key Laboratory for Mineral Deposits

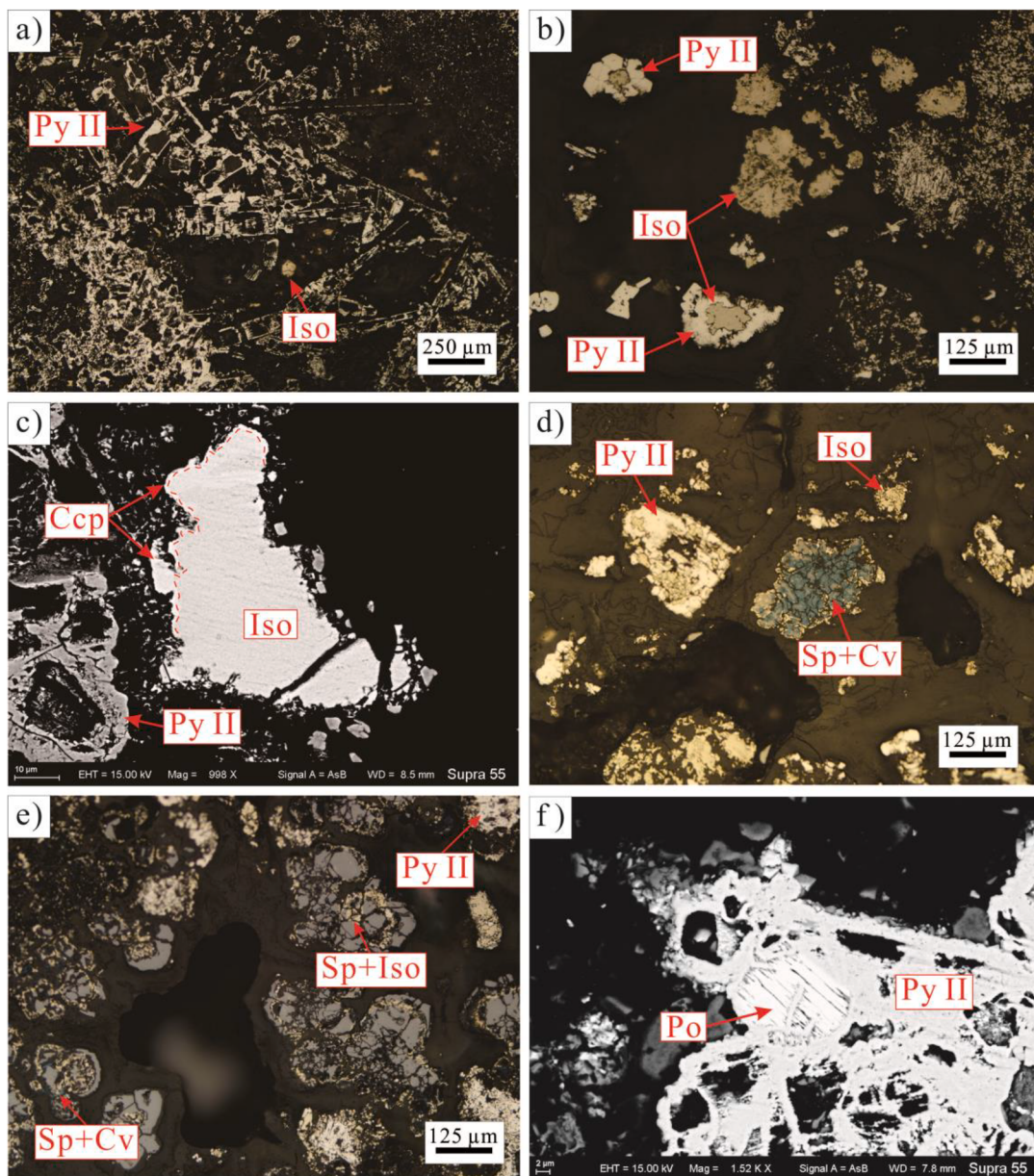


**Fig. 5.** Photomicrographs and BSE images of Tianzou isocubanite, sphalerite, and pyrrhotite showing: (a) coexistence of isocubanite with pyrite II showing pseudomorphic textures after pyrrhotite (reflected light); (b) isocubanite surrounded by pyrite II (reflected light); (c) typical grid textures of isocubanite through the exsolution of chalcopyrite (BSE image); (d) sphalerite replaced by covellite, coexisting with isocubanite surrounded by pyrite II (reflected light); (e) isocubanite present in sphalerite through exsolution, both coexisting with covellite (reflected light); (f) pyrrhotite replaced by pyrite II showing pseudomorphic textures after pyrrhotite (reflected light); Abbreviations: Py: pyrite; Iso: isocubanite; Ccp: chalcopyrite; Sp: sphalerite; Cv: covellite; Po: pyrrhotite.

Research, Nanjing University, Nanjing, China, with an accelerating voltage of 15 kV.

### 3.2. In situ LA-ICP-MS analysis

Based on the paragenetic sequence and morphology of sulfides, pure isocubanite (62 grains) and pyrite II (40 grains) without visible surface mineral inclusions were selected for *in situ* laser-ablation–inductively coupled plasma–mass spectrometry (LA-ICP-MS) determination of trace-element compositions. There were insufficient quantities of other sulfide minerals such as pyrrhotite, sphalerite, pyrite I, and covellite for such analyses. A Teledyne Cetac Technologies *Analyte Excite* laser-ablation system (Bozeman, Montana, USA) coupled to an Agilent Technologies 7700x ICP-MS instrument (Hachioji, Tokyo, Japan) was used, at Nanjing FocuMS Technology, Nanjing, China. The operating

conditions and methods of data reduction used are described by Xie et al. (2008), Hou et al. (2009), and Gao et al. (2013). In brief, the 193 nm ArF excimer laser, homogenized by a set of beam delivery systems, was focused on sulfide surface with fluence of 6.06 J/cm<sup>2</sup>. A 15 s gas background was collected prior to each ablation. Experimental Ablation protocol employed a spot diameter of 40 µm at 5 Hz repetition rate for 40 s (equating to 240 pulses). Helium carrier gas efficiently transport aerosol, and mixed with the Argon via a T-connector before entering the ICP-MS. USGS polymetal sulfide pressed pellet MASS-1 and synthetic basaltic glasses GSE-1G were combined calibration for sulfides (Gao et al., 2013). The standards were analyzed after every 10 spots to correct for instrument drift and mass discrimination. Raw data reduction were performed off-line by ICPMSDataCal software using 100%-normalization strategy without applying internal standard (Liu et al., 2008). Precision and accuracy were better than ± 10%.

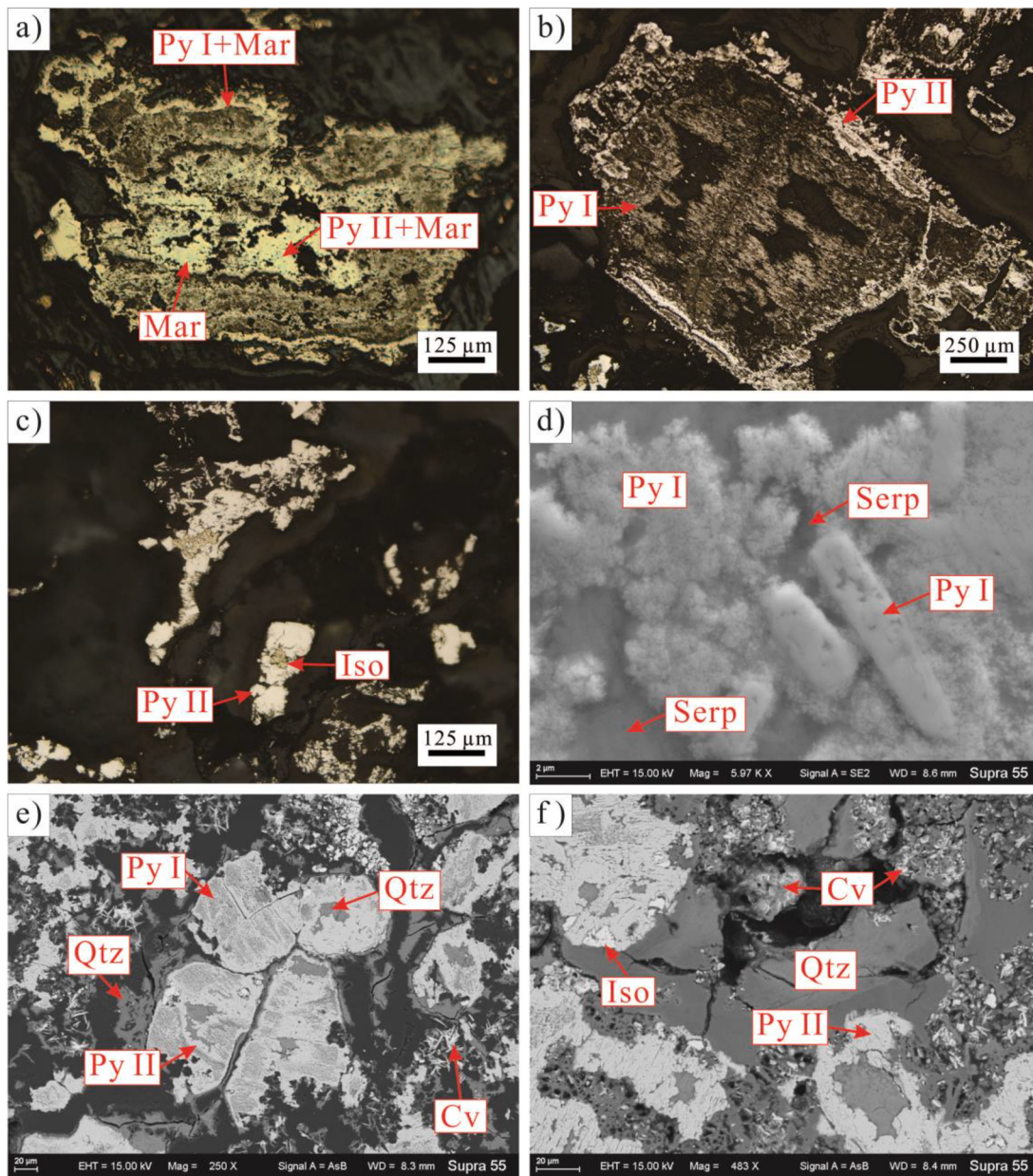


**Fig. 6.** Photomicrographs images of Tianzuo pyrite I, pyrite II, and covellite from the Tianzuo hydrothermal field: (a-b) pyrite I replacing pyrrhotite, showing pseudomorphic textures after pyrrhotite, which was further replaced by pyrite II (reflected light); (c) individual pyrite II grains replacing isocubanite (reflected light); (d) recrystallization of pyrite I (BSE image); (e) pyrite II contained in quartz veinlets, both of which growing around or replacing pyrite I (BSE image); (f) radial polycrystalline-textured covellite contained in quartz veinlets (secondary electron image). Abbreviations are as in Figs. 4 and 5, with Mar: marcasite; Qtz: quartz. Fig. 6a is quoted from Ding et al. (2021).

Care was taken during LA-ICP-MS analyses to choose analytical points free of surface inclusions, but the depth of penetration of the laser beam made their complete avoidance difficult, with small inclusions likely to be present within the volume of samples in some cases. The significance of this can be ascertained through inspection of time-resolved LA-ICP-MS depth profiles displayed as time-intensity scatterplots, which may be ragged, flat, or flat with occasional spikes, respectively indicating mineral inclusions, solid solutions or both.

### 3.3. Principal component analysis (PCA) of *in situ* datasets

In order to further understand the behaviors of trace elements within isocubanite and pyrite II, we processed log-transformed raw datasets of trace-element concentrations by the Principal Component Analysis

(PCA) module included in Matlab 7.11 software. All elements obtained by *in situ* LA-ICP-MS were selected and very few raw data below the detection limit were replaced by fixed value 0.01 which is close to the detection limitation of the analytical method (Van den Boogaart and Tolosana-Delgado, 2013; Yuan et al., 2018). The results of PCA applied to the datasets are shown as (1) loadings table with the eigenvector coefficients of the principal components; (2) histogram of the eigenvalues of principal components and their explained variability; (3) scatterplot showing the element distributions with higher correlation, and (4) bivariate graph illustrating the analyzed-spot distributions between the first two principal components.

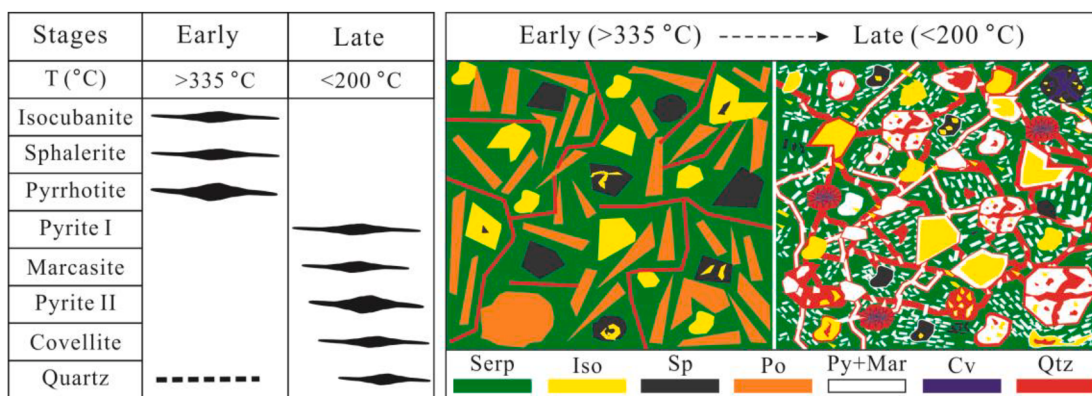


**Fig. 7.** Paragenetic sequence of minerals in the Tiansuo hydrothermal field. Sulfide mineralization includes early high- and late low-temperature stages. Mineral abbreviations are given in Fig. 6.

## 4. Results

### 4.1. Trace elements in sulfides

The trace-element contents of isocubanite and pyrite II from the Tiansuo hydrothermal field are presented in Supplementary Table 1, and summarized in Table 1. Isocubanite and pyrite II show distinct metal-distribution patterns in their time-resolved depth profiles, with the most concentrated metals having relatively flat profiles (Fig. 8a). It is clear that these sulfide phases are enriched in large ion lithophile elements (LILEs), such as Si, Mg, Al, Na, and K (Fig. 8a–c), with these elements exhibiting flat or spiked depth profiles indicating that they exist as uniformly distributed nanoparticles or silicate inclusions (Fig. 8a–c). However, metals such as Zn, Cu, Pb, Se, Sn, In, Co, and Mn display spiked depth profiles, indicating their occurrence as mineral inclusions (Fig. 8d–f). The depth profiles of some elements change simultaneously, such as for Cu, Pb, and Zn (Fig. 8d), Co, Cu, and Zn (Fig. 8e), Se, Sn, Pb, and In (Fig. 8e), and Co, Mn, and Cu (Fig. 8f), indicating that these elements probably have similar distributions in the sulfides. Trace elements can thus be divided into three groups according to their most likely form of occurrence in sulfide phases: Group 1 includes elements (e.g., Si, Mg, Al, Na, K, Ca, Rb, Sr, Ba, and W) that most likely occur as silicates or fluid inclusions in isocubanite and pyrite II; Group 2 includes elements that can substitute for major elements in isocubanite and pyrite II such as Fe and/or Cu (e.g., Pb, Zn, Co, Bi, Cd, Ag, In, Ni, Mn, and Sn) or S (e.g., Se and Te); and Group 3 includes elements that are closely associated with As and/or Sb (e.g., Au, Mo, V, Cr, Ga, Ge, Ti, and Tl). Each of these groups is discussed in detail below. In general, the isocubanite has similar concentrations for Group 1 and 3 elements compared with pyrite II, only except that Mo and Tl are enriched in the latter. On the contrary, all the Group 2 elements are more enriched in isocubanite than pyrite II.

#### 4.1.1. Group 1 elements

Both isocubanite and pyrite II from the Tiansuo hydrothermal field are enriched in LILEs, including Si (343–291,128 ppm), Mg (17–224,193 ppm), Al (< detection limit (<DL)–661 ppm), Na (2.25–7432 ppm), K (2.28–9169 ppm), Ca (<DL–2548 ppm), Rb (0.01–33.3 ppm), Sr (<DL–54.4 ppm), Ba (<DL–13.7 ppm), and W (<DL–2.75 ppm) (Table 1). These elements generally have much larger ionic radii compared with the major elements of isocubanite and pyrite (Fe, Cu, and S; Shannon, 1976), so they cannot incorporate the sulfide lattice by substitution. Their contents are also positively correlated with that of Si (Supplementary Fig. 1), and their time-resolved depth profiles change simultaneously. Therefore, it is likely that silicates occurred uniformly or as inclusions within sulfides (Fig. 8a–c). Magnesium is abundant in isocubanite (mean 45,640 ppm) and pyrite II (mean 26,575

ppm) and its content is positively correlated with that of Si (Supplementary Fig. 1a), indicating that serpentine is most likely one of the silicate inclusions in the sulfides. Aluminum is positively correlated with Si (Supplementary Fig. 1b), with a profile changing simultaneously with those of Si, Mg, Na, K, and Ca (Fig. 8a–e). The Al contents are low in both isocubanite (mean 33.2 ppm) and pyrite II (23.6 ppm), indicating the likely occurrence of Mg-bearing (e.g., pyroxene) or Na-, K-, and Ca-bearing Al silicate (e.g., feldspar) inclusions in the sulfides. Although pyrite II has higher Na, K, and Ca contents (means 1279, 1422, and 467 ppm, respectively) than those of isocubanite (812, 472, and 312 ppm, respectively), both sets are much higher than the Al contents of these sulfides, indicating that these elements occur not only as silicate inclusions (e.g., pyroxene or feldspar) but probably also as fluid inclusions of high salinity.

#### 4.1.2. Group 2 elements

Group 2 includes mainly the chalcophile and siderophile elements that are preferentially precipitated as sulfides, and minerals (mainly Se- and Te-bearing) similar to sulfides within both isocubanite and pyrite II. The element concentrations in isocubanite as: S (144,207–434,984 ppm), Fe (227,092–434,082 ppm), Se (13.2–540 ppm), Te (0.89–86.2 ppm), Cu (75,753–227,788 ppm), Zn (3116–15,236 ppm), Pb (1.23–84.5 ppm), Co (671–2078 ppm), Bi (0.05–3.65 ppm), Cd (4.12–88.7 ppm), Ag (0.87–3.84 ppm), In (0.95–21.6 ppm), Ni (0.70–238 ppm), Mn (693–2266 ppm), and Sn (5.42–11.3 ppm); whereas in pyrite II as: S (186,563–474,254 ppm), Fe (324,092–556,358 ppm), Se (<DL–69.9 ppm), Te (0.02–4.01 ppm), Cu (107–26,411 ppm), Zn (25.5–3996 ppm), Pb (0.03–17.9 ppm), Co (21.7–2043 ppm), Bi (0.01–0.64 ppm), Cd (0.07–3.73 ppm), Ag (0.01–3.28 ppm), In (0.01–0.80 ppm), Ni (0.36–31.4 ppm), Mn (146–3702 ppm), and Sn (<DL–2.73 ppm) (Table 1).

The Se contents are positively correlated with Te, indicating that they behave similarly to S when incorporated into sulfides (Fig. 9a). The Cu, Zn, Pb, Co, Bi, Cd, Ag, In, Ni, Mn and Sn contents are positively correlated with Se content (Figs. 9 and 10 and Supplementary Fig. 2), which is especially true for isocubanite, suggesting that they are also positively correlated with S contents, with these elements existing most likely as S-dominated minerals in sulfides. The depth profiles of Cu, Zn, Pb, Co, Mn, Sn, Se, and In change simultaneously (Fig. 8d–f), further suggesting similar behaviors when substituting into sulfides. Among these Group 2 elements, some element pairs can be further distinguished based on the significantly positive correlations between their contents, suggesting the exactly similar behaviors for these elements when substituting into the sulfide lattices, such as Se–Te ( $R^2 = 0.85$ ), Cu–Zn ( $R^2 = 0.86$ ), Zn–Cd ( $R^2 = 0.61$ ), and Sn–In ( $R^2 = 0.78$ ) (Figs. 9 and 10).

The Zn contents of all analyzed isocubanite grains from the Tiansuo hydrothermal field exceed 2000 ppm, with some pyrite II grains also

**Table 1**  
*In-situ* LA-ICP-MS trace-element concentrations of isocubanite and pyrite II from the Tiansuo hydrothermal field. This data set is part of the electronic material.

Sulfide types	Fe (ppm)	S (ppm)	Cu (ppm)	Na (ppm)	Mg (ppm)	Al (ppm)	Si (ppm)	K (ppm)	Ca (ppm)	Rb (ppm)	Sr (ppm)	Ti (ppm)	V (ppm)	Cr (ppm)	Mn (ppm)	Pb (ppm)	Co (ppm)	Ni (ppm)	
Isocubanite (N = 62)	227,092	144,207	75,753	2.25	16.7	0.06	343	2.28	3.41	0.01	<DL	<DL	0.07	693	1.23	671	0.70		
	Max	434,082	434,984	227,788	5,463	224,194	661	287,282	3656	1357	14.1	17.1	40.6	8.38	157	2266	84.5	2078	238
	Average	367,709	343,219	169,990	812	45,640	33.7	60,087	472	339	1.69	3.99	2.68	1.46	9.84	1298	7.02	1402	13.8
	S.D.	43,545	54,408	35,691	960	52,864	105	60,113	662	275	2.45	3.89	7.50	1.51	20.8	345	12.6	391	30.4
Pyrite II (N = 40)	Min	324,352	186,563	107	64.5	84.1	<DL	563	25.4	25.8	0.05	0.7	<DL	0.01	<DL	146	0.03	22	0.36
	Max	556,358	474,254	26,411	7433	186,676	274	291,129	9169	2548	54.4	9.52	5.97	10.3	103	3702	17.9	2043	31.4
	Average	500,609	403,836	3452	1279	26,575	23.6	59,958	1422	467	4.56	10.8	1.44	1.32	7.05	1157	2.03	332	6.49
	S.D.	48,322	67,292	5791	1440	37,336	51.4	71,097	2058	493	7.22	10.9	1.96	1.49	17.1	821	3.72	440	7.51
Sulfide types	Isocubanite (N = 62)	Zn (ppm)	Ga (ppm)	Ge (ppm)	As (ppm)	Se (ppm)	Mo (ppm)	Ag (ppm)	Cd (ppm)	In (ppm)	Sn (ppm)	Sb (ppm)	Te (ppm)	Ba (ppm)	W (ppm)	Au (ppm)	Tl (ppm)	Bi (ppm)	
		3116	0.05	6.98	>DL	13.2	0.05	0.87	4.12	0.95	5.42	<DL	0.89	0.01	<DL	0.01	<DL	0.05	
		Max	15,236	3.42	13.9	167	540	19.3	3.84	88.7	21.6	11.3	2.16	86.2	5.05	0.92	4.06	1.61	
		Average	8708	0.32	10.2	10.7	198	5.78	1.78	16.4	4.03	7.96	0.31	24.9	0.71	0.09	0.19	0.15	
Pyrite II (N = 40)		S.D.	3034	0.47	1.44	24.7	128	4.40	0.66	13.1	3.46	1.32	0.39	17.2	0.93	0.14	0.55	0.27	0.47
		Min	25.5	<DL	10.1	<DL	2.36	0.01	0.07	0.01	<DL	0.02	0.02	0.16	<DL	0.01	0.03	0.01	
		Max	3996	2.16	18.1	16.9	69.9	37.6	3.28	3.73	0.80	2.73	5.01	4.01	13.6	2.75	2.62	0.67	
		Average	810	0.17	12.4	3.83	13.0	10.6	0.49	0.88	0.11	0.68	0.91	0.45	1.44	0.19	0.26	0.14	
		S.D.	924	0.34	1.80	3.81	14.3	8.04	0.67	0.79	0.16	0.67	1.18	0.72	2.28	0.45	0.57	0.12	

Note: <DL: below detection limit; S.D: standard deviation.

having Zn contents >2000 ppm (although most are lower). In addition, the Zn depth profile changes simultaneously with that of Cu in both pyrite II and isocubanite (Fig. 8d–e), suggesting that Zn substituted into isocubanite together with Cu. The high and variable Zn contents of pyrite II most likely reflect the occurrence of isocubanite inclusions in this sulfide (Fig. 8d). The Cd contents are positively correlated both with Se and Zn contents (Fig. 9f and Fig. 10b), indicating that these two elements may be incorporated similarly into sulfides (in particular, sphalerite) (e.g., Cook et al., 2009; Belissent et al., 2014).

The roughly positive relationship between Co and Ni contents in pyrite II indicates that these elements substitute in pyrite by similar ways. The Ni contents have an obviously negative relationship with Co contents in isocubanite, and this most likely results from substitution of Co for Ni when the contents of Co are elevated (Fig. 10c). The Mn contents are positively correlated with Co contents in both isocubanite and pyrite II (Fig. 10d), and depth profiles of Co and Mn change simultaneously in pyrite II (Fig. 8f), suggesting that these elements behave similarly when substituting into sulfides.

The depth profiles of Pb and Zn change simultaneously (Fig. 8d), suggesting that these Pb and Zn behave similarly when substituting into sulfides (Fig. 10e). No Pb-bearing sulfides are observed in the Tiansuo hydrothermal field, the positive relationships between Pb, Bi, and Ag contents suggest that Bi and Ag most likely exist in Bi-rich and argentiferous galena inclusions (Fig. 10f and Supplementary Fig. 2f).

Roquesite ( $\text{CuIn}_2\text{S}_2$ ) is isostructural with chalcopyrite (Wittmann, 1974), and Sn can substitute for Fe in stannite ( $\text{Cu}_2\text{FeSn}_4\text{S}_4$ ), which has a similar crystal structure to that of chalcopyrite (Wuensch, 1976). Indium and Sn therefore may also be incorporated into isocubanite and pyrite II by substituting for Fe as they are positively correlated in both sulfides (with a trend sub-parallel to the In/Sn = 1 line; Fig. 10g).

The Ag contents have no obvious correlation with Au in either isocubanite or pyrite II (Supplementary Fig. 2a), indicating that they do not exist as electrum ( $\text{AgAu}$ ) in sulfides. Nor is Ag correlated with Sb (Supplementary Fig. 2h), suggesting a lack of inclusions enriched in both Ag and Sb, such as argentiferous tetrahedrite ( $(\text{Cu}, \text{Fe})_{12}\text{Sb}_4\text{S}_{13}$ ). Silver is positively correlated with Te, Zn, and Pb (Supplementary Fig. 2b, d, f), indicating that Ag probably occurs in sulfides in forms similar to those of other chalcophile elements, such as argentite ( $\text{Ag}_2\text{S}$ ). The relative higher Se and Te contents of isocubanite than pyrite II indicate the possible occurrence of naumannite ( $\text{Ag}_2\text{Se}$ ; Fig. 9g) and hessite ( $\text{Ag}_2\text{Te}$ ; Supplementary Fig. 2b) in the former.

#### 4.1.3. Group 3 elements

Group 3 elements include Au (<DL–4.06 ppm), As (<DL–167 ppm), Sb (<DL–5.01 ppm), Mo (0.05–37.7 ppm), V (<DL–8.38 ppm), Cr (<DL–157 ppm), Ga (<DL–3.42 ppm), Ge (6.98–18.1 ppm), Ti (<DL–40.6 ppm), and Tl (<DL–1.61 ppm) (Table 1). These elements display no positive correlations with S, Se, or Te in both isocubanite and pyrite II (Fig. 10h), meaning that they are not incorporated into sulfides as S-, Se-, or Te-bearing minerals. However, they do have roughly positive relationships with As and Sb (Supplementary Fig. 2e, g and Supplementary Fig. 3), indicating that As- and/or Sb-bearing minerals most likely account for most of these elements in both isocubanite and pyrite II.

The Au contents are positively correlated with As and Sb contents (Supplementary Fig. 2e, g), and, as As has negative and positive relationships with Se and Sb, respectively (Fig. 10h and Supplementary Fig. 3a), Au might occur in sulfides in As- or Sb-bearing minerals such as aurostibite ( $\text{AuSb}_2$ ). Arsenic is the most common nonstoichiometric substitution in pyrite lattice, with values of up to 8 wt% (Fleet et al., 1989). Cook and Chryssoulis (1990) proposed a model for  $[\text{Metal}]^{3+}(\text{AsS})^{3-}$  substitution for  $\text{Fe}^{2+}(\text{S}_2)^{2-}$  in sulfides, with As substitution in the pyrite lattice occurring when  $(\text{AsS})^{3-}$  anions substitute for  $(\text{S}_2)^{2-}$  anions, as indicated by the negative relationship between As and Se (Fig. 10h). This substitution forms a lattice site that trivalent metal ions such as  $\text{Fe}^{3+}$  and  $\text{Au}^{3+}$  may occupy. Regarding Sb, although tetrahedrite

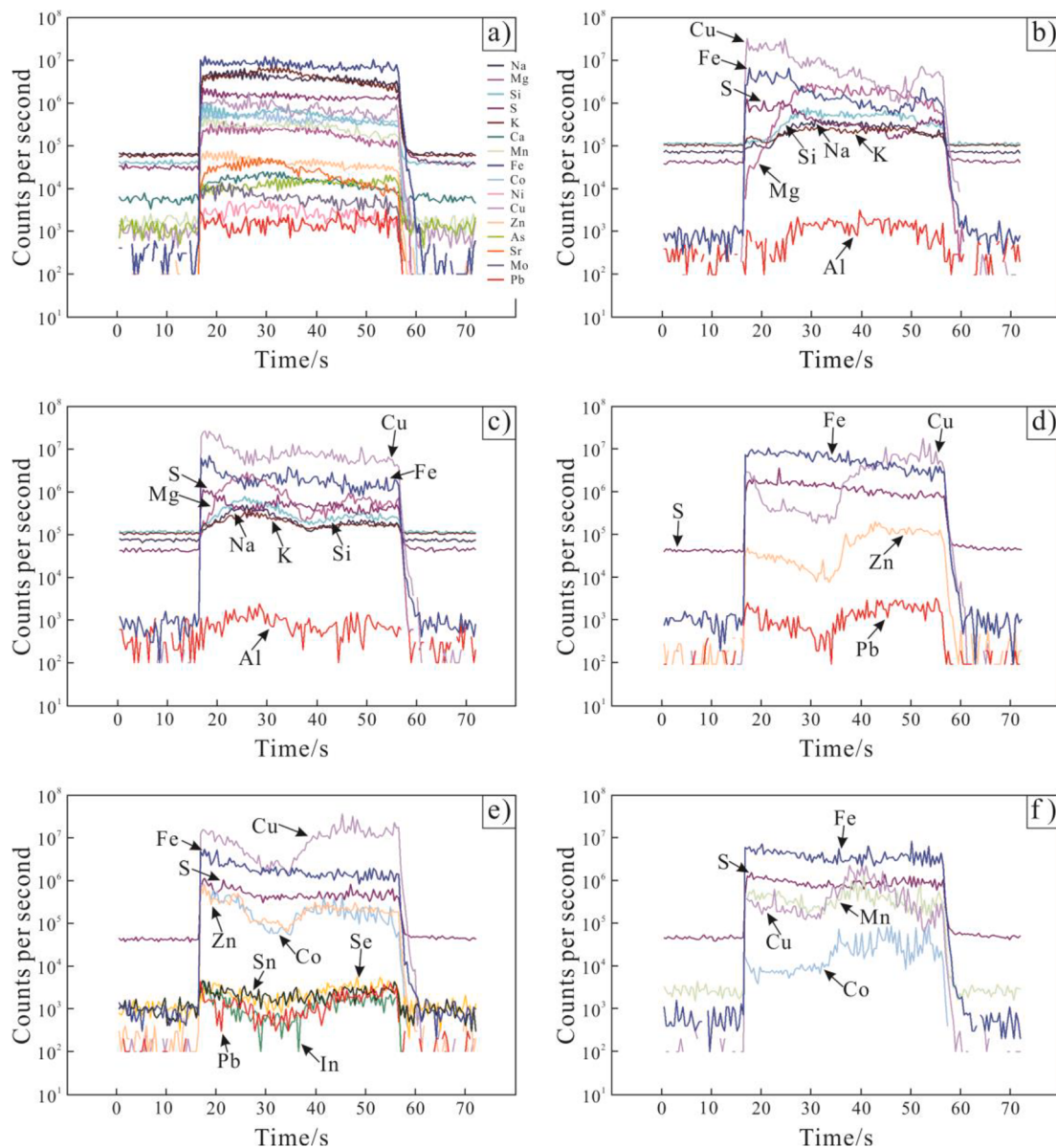


**Fig. 8.** Time-resolved LA-ICP-MS analytical signals: (a) signals of pyrite where silicate exists in sulfides as uniformly distributed nanoparticles; (b–f) signals of isocubanite and pyrite containing silicate or sulfide inclusions.

can account for most Sb in sulfides, Sb is also positively correlated with As (Supplementary Fig. 3a), so may behave similarly to As in the sulfides as well.

Other Group 3 elements include Mo, V, Cr, Ga, Ge, Ti, and Tl, the extremely low concentrations for these elements make the correlations with element As weak. No Mo-bearing minerals were observed optically in sulfides from the Tianzuo hydrothermal field, and Mo shows no correlation with S, so it does not seem to occur in sulfides as Mo-bearing mineral inclusions such as molybdenite. Under reducing conditions, molybdenum occurs as Mo<sup>3+</sup> and could be accommodated in the structure of pyrite according to the model of Cook and Chryssoulis (1990), similar to Au<sup>3+</sup> as mentioned above, as evidenced by the roughly positive relationship between Mo and As (Supplementary Fig. 3b).

Although Ga can substitute Fe and form gallite inclusions (CuGaS<sub>2</sub>), this element displays no positive correlation with Cu or S, so gallite inclusions are not expected in sulfides; rather, Ga contents have a roughly positive relationship with As and Sb contents (Supplementary Fig. 3c), which means that Ga in sulfides from the Tianzuo hydrothermal field is associated with As or Sb.

Quadrivalent Ge<sup>4+</sup> can substitute into sulfide coupled with divalent metals, such as this element can substitute 3Zn<sup>2+</sup> by coupled with Cu<sup>2+</sup> in sphalerite (Belissont et al., 2014). However, this element shows no positive correlation with Cu; instead, Ge contents have a roughly positive relationship with As and Sb contents (Supplementary Fig. 3d), this is interpreted as that Ge most likely in sulfides from this hydrothermal field is related with As or Sb, as it has the similar behaviors to the element Ga, with the possible substitution mechanism as follow:



Although V-, Cr-, Ti-, and Tl-bearing sulfide minerals have not been observed in the Tianzuo hydrothermal field, and although the mechanisms of substitution of these elements in sulfides are unclear, they display roughly positive relationships with As (Supplementary Fig. 3e-h). This suggests that these elements were also most likely substituted into the sulfide lattice as trivalent ions (V<sup>3+</sup>, Cr<sup>3+</sup>, Ti<sup>3+</sup>, and Tl<sup>3+</sup>), consistent with [Metal]<sup>3+</sup> in the model proposed by Cook and Chryssoulis (1990).

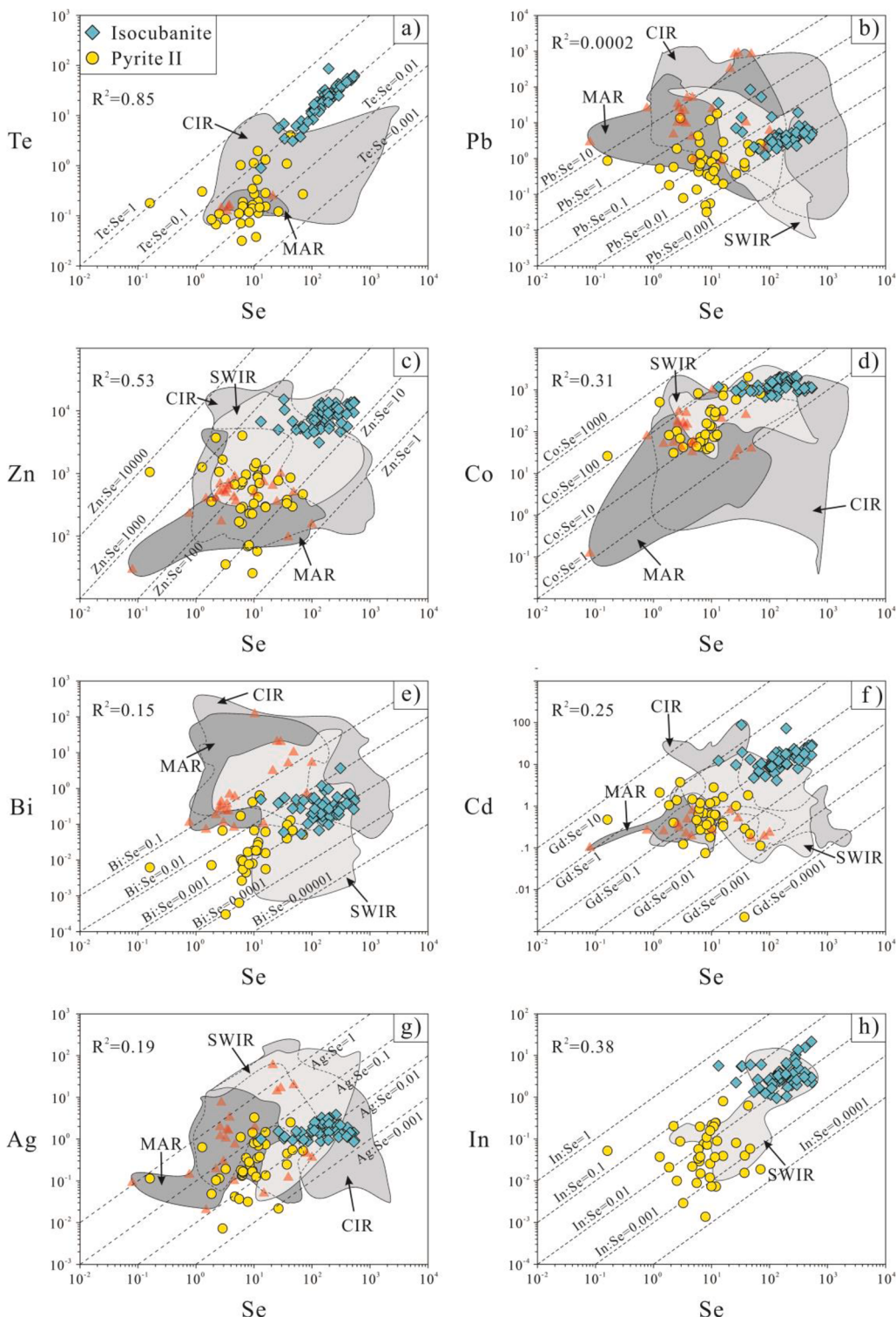


**Fig. 9.** Bivariate graphs showing the relationships between Se and other trace-element contents: (a) Te–Se; (b) Pb–Se; (c) Zn–Se; (d) Co–Se; (e) Bi–Se; (f) Cd–Se; (g) Ag–Se; (h) In–Se. Data sources for MAR, CIR, and SWIR in Figs. 10–13 are from Keith et al. (2016) and Yuan et al. (2018), concentrations of pyrite from typical ultramafic-hosted Logatchev field are also shown as red triangles.

#### 4.2. Principal component analysis

The results of the PCA applied to the datasets are shown in Fig. 11, including loadings (Fig. 11a), explained variance (Fig. 11b), element distributions (Fig. 11c), and analyzed-spot distributions (Fig. 11d). Elements and spot analyses are projected on the PC1–PC2 plane and account for 63.1% of element-content variance. Element distributions

highlight four main groups or element correlation clusters (Fig. 11c), termed groups A, B, C, and D. Group A comprises Cu and the trace elements Te, Se, In, Cd, Ag, Co, Zn, Sn, Pb, Bi, Mn, and Ni (loading on PC1). These elements are incorporated into sulfides by substitution of S and Fe, and are generally enriched in isocubanite than pyrite II. Group B comprises Mg and other LILEs including Si, Al, Sr, K, Rb, Na, Ca, Ba, and W (loading on PC2), which resulted from the contamination of silicates

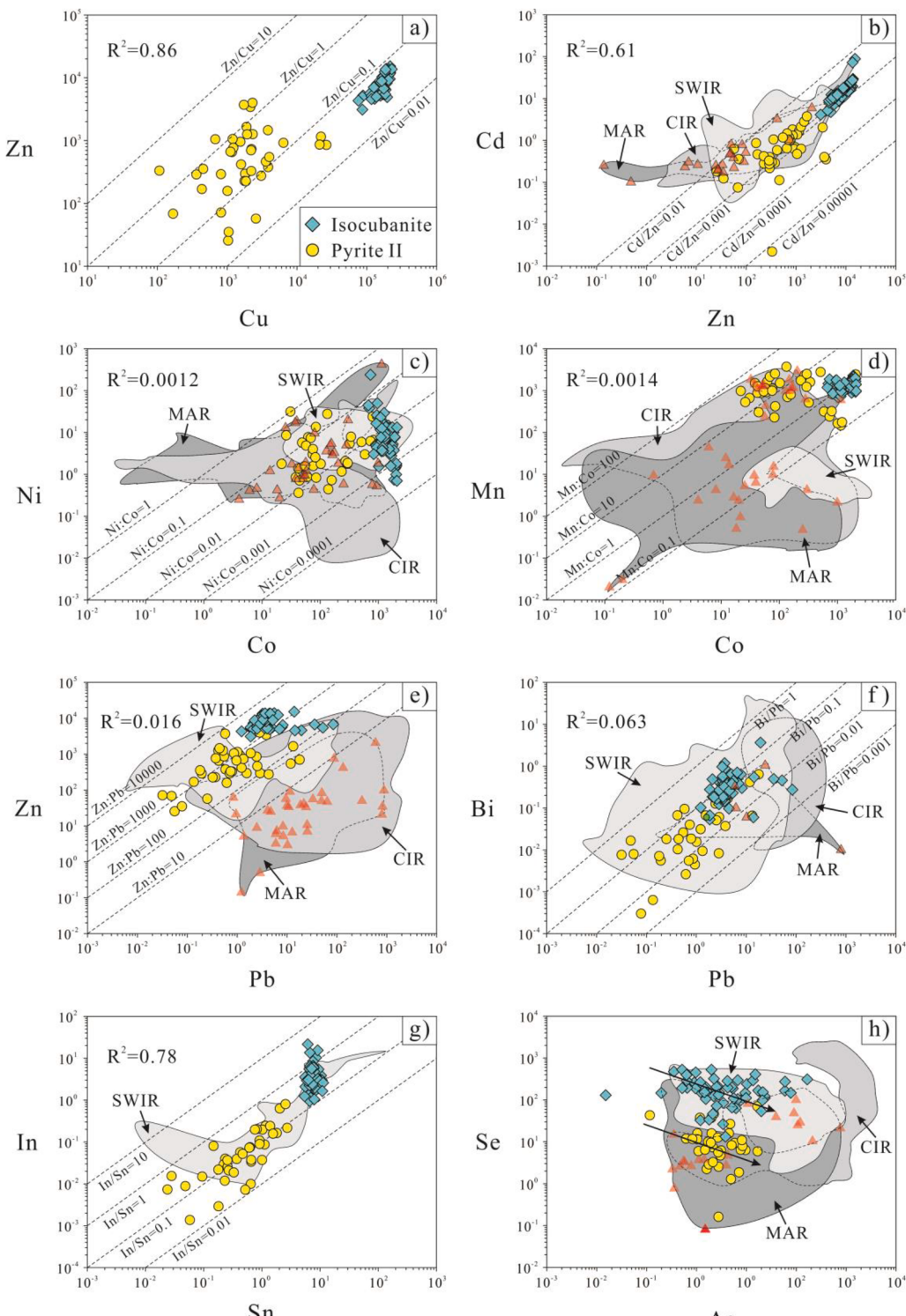


**Fig. 10.** Bivariate graphs showing the relationships between trace-element contents: (a) Zn–Cu; (b) Cd–Zn; (c) Ni–Co; (d) Mn–Co; (e) Zn–Pb; (f) Bi–Pb; (g) In–Sn(b); (h) Se–As.

in the process of analyses, and are generally enriched in both isocubanite and pyrite II. Group C comprises As, Sb, Mo, Au, Cr, Ti, V, Ga, Tl and Ge<sub>2</sub> with this group occupying an intermediate position between group A along PC1 and group B along PC2, and with these elements occurring as arsenides or stibnides in sulfides. The Groups A, B, and C illustrated by the PCA have significantly highlighted the strong correlation between the Groups 2, 1, and 3 elements as described in the section above. Group D comprises Fe and S, which exhibit a relatively well-marked negative

correlation with both PC1 and PC2, most likely because Fe and S are the major elements in the lattices of both isocubanite and pyrite and are commonly substituted by other elements with similar behaviors in sulfides (Fig. 11c). The pattern of individual spot analyses of the different elements on the PC1–PC2 plane illustrated in Fig. 11d corresponds to different types of sulfides: isocubanite is positively correlated to PC1 (group A elements), whereas pyrite II is against PC1. Both of isocubanite and pyrite II are correlated to PC2 (loaded by group B elements).

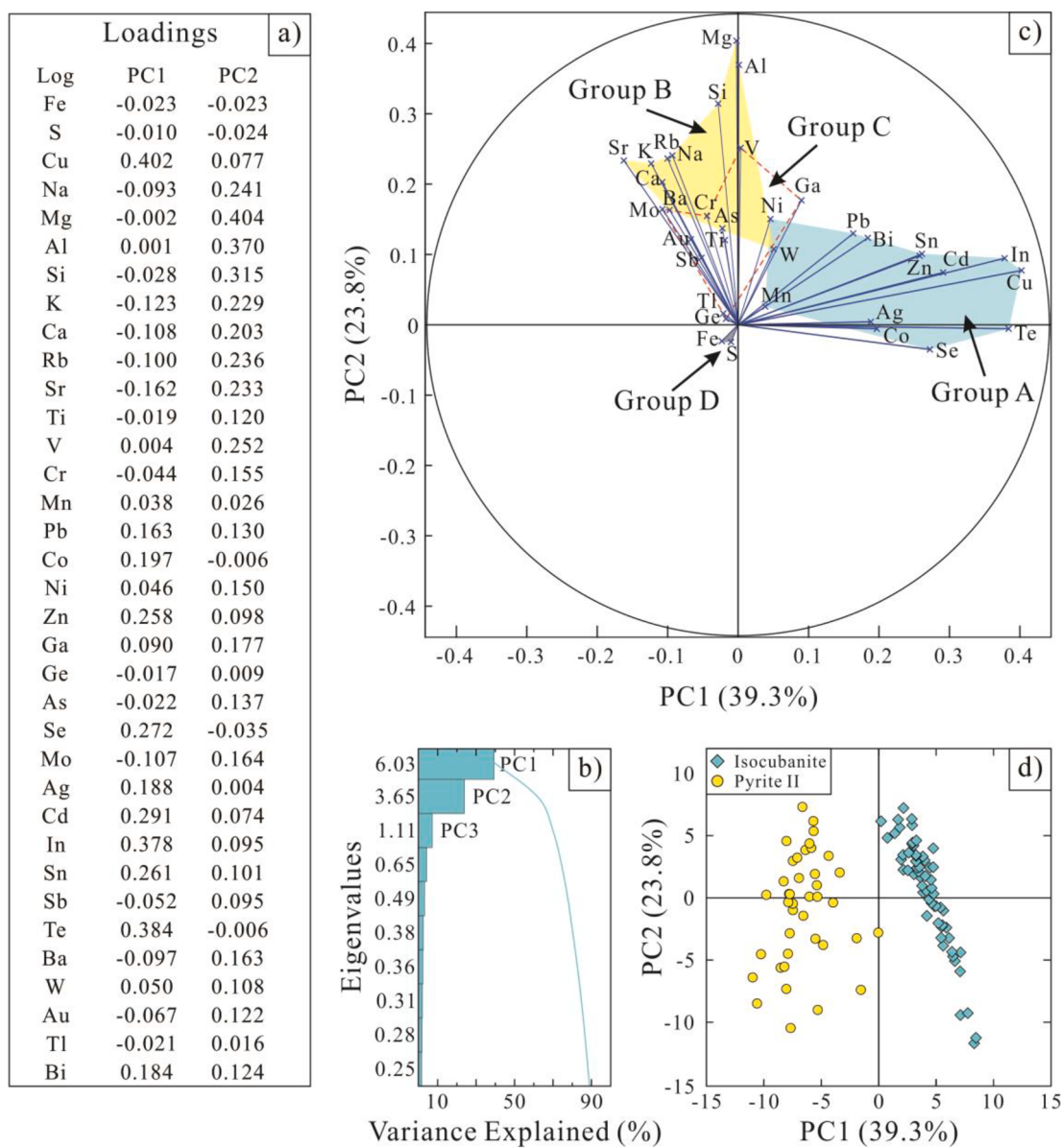


**Fig. 11.** PCA of the log-transformed datasets of trace-element contents of isocubanite and pyrite from the Tianzuo hydrothermal field: (a) loadings; (b) variance explanation of the principal components; (c) elements plotted in the PC1–PC2 plane (explaining 63.1% of element-content variability); (d) individual spot analyses of the different elements plotted in the same plane.

## 5. Discussion

### 5.1. Heat sources for high- and low-temperature sulfide mineralization hosted in ultramafic rocks

Numerous studies attempt to explain the composition and physico-chemical conditions of ore-forming fluids based on the sulfide minerals compositions. This is especially true for the modern seafloor hydrothermal fluids associated sulfide deposits, which rarely experience late recrystallization and metamorphism that can significantly modify the primary trace element distributions (e.g., Halbach et al., 1998; Butler and Nesbitt, 1999; Houghton et al., 2004; Li et al., 2012; Melekestseva et al., 2014; Melekestseva et al., 2017; Wohlgemuth-Ueberwasser et al., 2015; Keith et al., 2016; Dekov et al., 2018; Grant, et al., 2018). Trace-element compositions in the sulfide phases can be controlled by several conditions of the hydrothermal systems, such as temperature, pH, redox conditions, and composition of the hosted rocks (e.g., Huston et al., 1995; Grant, et al., 2018). Moreover, the intervention of other processes

occurring during the hydrothermal circulation, for example, the phase separation of the fluids or the direct contribution of magmatic sources may also contribute directly for the compositions of sulfides (e.g., Herzig et al., 1998). In sulfide phases, trace elements may occur in the chemical structure solid solutions, submicroscopic mineral inclusions, or by adsorption onto sulfide surfaces (e.g., Cook, 1996; Cook et al., 2009). Several factors may control the partition coefficient of trace elements between sulfides and hydrothermal fluids, including the size of the cation site in which substitution may occur, the charge-balance mechanism that allows the trace element to enter the sulfide lattice, and the nature of the trace element in the hydrothermal fluids (Goldschmidt's First Rule; Ghaderi et al., 1999; Ding et al., 2018a; Ding et al. (2018b)). Since isocubanite and pyrite have similar formulas as CuFe<sub>2</sub>S<sub>3</sub> and FeS<sub>2</sub>, respectively, this means that except for those directly substitute for Cu in the isocubanite, the other elements most likely enter these two sulfide minerals in similar ways by substituting S and Fe, sites available for trace-element substitution in these two sulfides are therefore most likely similar, and thus trace-element contents of isocubanite and pyrite are

predominantly controlled by the composition and physicochemical condition of ore-bearing hydrothermal fluids rather than by the differences between their crystal features.

Serpentinization of ultramafic rocks was one of the heat sources driving hydrothermal circulation in sulfide and non-sulfide hydrothermal fields, however, heat-balance models predict that a wide range of hydrothermal venting temperatures may result from serpentinization reactions of peridotite, but temperatures of the hydrothermal fluids triggered by this process are only 40–75 °C (Lowell and Rona, 2002). The occurrence of pyrrhotite and isocubanite during early-stage sulfide mineralization in the Tiansuo hydrothermal field suggests that the temperature of hydrothermal fluids could be as high as 335 °C (Lusk and Bray, 2002), much higher than those developed through serpentinization reactions of peridotites. Unlike the other SWIR hydrothermal fields, there has been very little eruption of basalt in the ridge segment where the Tiansuo hydrothermal field is located (Fig. 2a). It is therefore likely that gabbroic intrusions occur beneath this field, with these providing additional heat. In fact, the occurrence of oceanic core complexes means that at least part of the oceanic lithosphere formed at slow- and ultraslow-spreading centers comprises peridotite with gabbroic intrusions in varying proportions (Cannat, 1996; Ranero and Reston, 1999; Lowell and Rona, 2002; Ildefonse et al., 2007). This suggest that gabbroic intrusions might provide additional heat necessary for mineralization in the Tiansuo hydrothermal field. High rates of serpentinization, episodically triggered by tectonic activity or fracture propagation, may produce hydrothermal fluids with temperatures of up to ~300 °C (Wetzel and Shock, 2000), but such fluids produced by serpentinization of different volumes of fresh lithosphere must have similar metal compositions derived from homogeneous initial rocks (e.g., ultramafic rocks and serpentinite). However, isocubanite and pyrite II of the Tiansuo hydrothermal field have distinct Te/Se, Cu/Zn, Co/Ni, Co/Mn, and In/Sn ratios (Fig. 10a and 11a, c–d, g), and the more elevated Te, Cu, Co, and In in isocubanite (compared with Se, Zn, Ni, Mn, and Sn) most likely derived from the gabbroic intrusions. Combination, we consider that the heat sources for the high- and low-temperature sulfide mineralization within Tiansuo field might be different, with the intrusion of gabbro dominated the heat source for the high-temperature stage, including isocubanite, sphalerite, and pyrrhotite; while the serpentinization of ultramafic rocks by the reaction with seawater might be the heat source for the low-temperature sulfide mineralization, including pyrite I, II, and covellite.

### 5.2. Possible sources of metals and ore-forming fluids for high- and low-temperature sulfide mineralization

Compared with other seafloor hydrothermal sulfide deposits along sediment-starved oceanic ridges, including the TAG and Logatchev deposits of the MAR, the Meso Zone and Kairei deposits of the CIR, and the Longqi deposit of the SWIR (Keith et al., 2016; Yuan et al., 2018), both isocubanite and pyrite II in the Tiansuo field (especially isocubanite) are generally enriched in the trace elements Se, Te, Zn, Co, Ni, and Mn, and depleted in Pb, Bi, Ag, Au, Sb, and As (Figs. 9 and 10 and Supplementary Figs. 2 and 3). Variations in concentrations of these elements in the studied sulfide minerals indicate that hydrothermal fluids where sulfides were precipitated were either enriched or depleted in these elements compared with those in other oceanic ridges. Three end-members may have contributed to the compositions of hydrothermal fluids where sulfides were precipitated within ultramafic rocks: ultramafic rocks from which elements were leached during serpentinization; seawater; and gabbroic intrusions (Herzig et al., 1998; Wetzel and Shock, 2000; Douville et al., 2002; Charlou et al., 2002; Seal, 2006). Although isocubanite and pyrite II have distinct elemental contents, most of the above elements have positive correlations or roughly positive relationships within these two sulfides, except for Ge, Au, Ni, Mo, and Tl (Figs. 9 and 10 and Supplementary Figs. 2 and 3). Their distinct compositions but positive relationships indicate that isocubanite and pyrite II are likely to have

similar sources of ore-forming metals such as Pb, Zn, Bi, Cd, Ag and Sn.

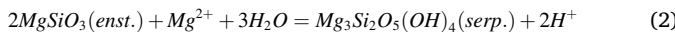
Pyrite II is substantially more enriched in Mo and Tl than isocubanite, these elements generally occur as arsenides or stibnides in sulfides, and are generally enriched as in seawater rather than hydrothermal fluids (Douville et al., 2002; Schmidt et al., 2007), indicating that hydrothermal fluids where pyrite II precipitated were significantly affected by low-temperature seawater. In contrast, isocubanite precipitated in high-temperature environments and has higher Te/Se, Cu/Zn, Co/Ni, Co/Mn, and In/Sn ratios than those of pyrite II, these distinct ratios cannot be fully controlled by temperature, as isocubanite is most likely enriched of all the elements Co, Se, Bi, Cu, Ni, and Sn under high temperature (e.g., Grant, et al., 2018). Sources of isocubanite-precipitating hydrothermal fluids thus have relative higher Te, Cu, Co, and In contents (compared with Se, Zn, Ni, Mn, and Sn) than those where pyrite II precipitated, which were likely contributed by injection of basaltic magmas beneath the Tiansuo hydrothermal field. Previous studies have shown that in addition to basalts, peridotites form a significant portion of the upper oceanic crust in slow- and ultraslow-spreading environments, with basaltic lavas occurring only as a thin veneer and with basaltic magmas locally being injected into peridotites (Dick, 1989; Cannat, 1993; Cannat, 1996; Dick et al., 2003; Standish and Sims, 2010; Zhou and Dick, 2013). In the Tiansuo hydrothermal field, intrusion of gabbroic magma may also break the crust and increase the volume of fresh lithosphere accessible to serpentinization (Lowell and Rona, 2002; Ildefonse et al., 2007), enhancing the serpentinization reactions and extraction of majority metals from ultramafic rocks, with isocubanite precipitated during this stage being more enriched in most metals than late-stage pyrite II. Gabbroic intrusions may thus have provided additional fluids and metals for hydrothermal fluids where isocubanite precipitated, whereas pyrite II precipitation was dominated by the relative weak serpentinization reaction between ultramafic rocks and seawater.

If hydrothermal fluids where isocubanite and pyrite II precipitated were influenced by different sources, distributions of distinct endmembers should be significantly discriminated by PCA (Belissoent et al., 2014, and references therein; Yuan, et al., 2018; Meng et al., 2019). We processed log-transformed raw datasets of trace-element contents by PCA to distinguish metal sources for isocubanite and pyrite II (Fig. 11). The first discrimination factor, PC1, was loaded with Cu, Te, In, and other trace elements with similar behaviors including Cd, Se, Sn, Zn, Co, Ag, Bi, Pb, Mn, and Ni; and the second factor, PC2, was loaded with Mg, Al, Si, and other LILEs including Sr, K, Rb, Na, Ca, Ba, and W (Fig. 11c). The PC1–PC2 plot indicates that isocubanite and pyrite II are dominated by PC1 and against PC1, respectively, both of these sulfides are significantly influenced by PC2 (Fig. 11d). This means that hydrothermal fluids where isocubanite precipitated were enriched in Cu, Te, In, and similar metals, with these elements generally being incorporated into isocubanite by substitution or through mineral inclusions. Their high concentrations indicate intense serpentinization with additional magmatically derived hydrothermal fluids as proposed above. Pyrite II is depleted in the elements loading on PC1, and enriched in Mo and Tl, indicating precipitation from hydrothermal fluids controlled predominantly by seawater convection rather than the influences of magmatic fluids. Fig. 11d thus illustrates the difference between additional metal sources: magmatic (PC1: right side) and lack of magmatic (against PC1: left side). However, the concentrations of LILEs in isocubanite and pyrite II are both significantly influenced by serpentinization of ultramafic rocks (PC2: top side), which are resulted from the contamination of silicates during the process of analyses as mentioned before.

### 5.3. Role of serpentinization in sulfide mineralization hosted in ultramafic rocks

The compositions of hydrothermal fluids are determined by their ability to extract metals, which is dominated by physicochemical conditions such as temperature, pH, the ligands involved, and redox con-

ditions (Von Damm, 1990; Seyfried and Ding, 1993; Seyfried and Ding, 1995; Pokrovski et al., 2008; Hannington, 2014). Previous studies have indicated that hydrothermal fluids in ultramafic systems are generally of high temperature and low pH, with metals (particularly transition metals) being transported by chloro complexes under reducing conditions (Janecky and Seyfried, 1984; Seyfried and Ding, 1993; Seyfried and Ding, 1995; Douville, 1999; Douville et al., 2002; Keith et al., 2016). Such reactions, often involve serpentinization of olivine and orthopyroxene, releasing substantial quantities of H<sup>+</sup>. For example, the alteration of orthopyroxene enstatite (enst.) to serpentine (serp.), conserving Si, can be expressed as:

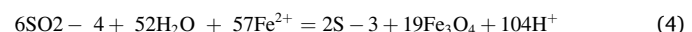
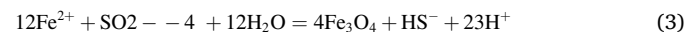


The H<sup>+</sup> released by such reactions may lead to an increase in Fe and other transition metal concentrations in hydrothermal fluids by promoting magnetite dissolution (Janecky and Seyfried, 1984; Jean-Baptiste et al., 1991; Wetzel and Shock, 2000; Charlou et al., 1998, 2002; Douville et al., 2002; Schmidt et al., 2007). The high temperatures of hydrothermal fluids resulting from the intrusion of gabbroic magma may enhance serpentinization by providing abundant magmatic fluids and volatiles to the hydrothermal systems (Ildefonse et al., 2007), providing heat to strengthen hydrothermal circulation, and exposing new reaction surfaces.

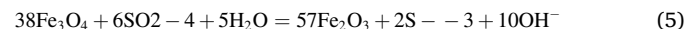
Hydrothermal fluids where isocubanite precipitated in Tianzuo hydrothermal field were significantly influenced by gabbroic intrusions and intense serpentinization reactions of ultramafic rocks, as discussed in the preceding section. These fluids are extremely enriched in metals (e.g., Cu, Zn, Se, Te, Pb, Co, Bi, Cd, Ag, In, Mn, and Sn; Figs. 9 and 10 and Supplementary Fig. 2) compared with those where pyrite II precipitated, as indicated by their concentrations in these two sulfides. It is difficult to identify the specific factors controlling the distributions of trace elements in isocubanite, but earlier studies have shown that these metals are generally transported as chloro complexes at low pH and high temperatures under moderately to strongly reducing conditions. Such as, Co (and probably Ni and Mn) and particularly Se (and probably S and Te) are strongly partitioned into pyrite at high temperatures (>300 °C) under such reducing conditions (e.g., Yamamoto et al., 1984; Auclair and Fouquet, 1987; Huston et al., 1995; Hannington et al., 1999a; Hannington et al. (1999b); Schmidt et al., 2007; Maslenikov et al., 2009, 2017; Revan et al., 2014; Genna and Gaboury, 2015; Keith et al., 2016; Grant, et al., 2018); whereas Zn, Cd, Co, and Mn, and probably Pb, Bi, and Ag, strongly favor chloro complexation under low-pH and high-temperature conditions (Douville et al., 2002). Sn (and probably In) is most effectively transported as a chloro complex in acidic, reduced hydrothermal fluids at high temperatures, and is most abundant in pyrite containing micro-inclusions of chalcopyrite (Heinrich and Eadington, 1986; Heinrich 1990; Huston et al., 1995; Hannington et al., 1999a; Grant et al., 2015). Therefore, serpentinization reactions of ultramafic rocks at high temperatures significantly enhance metal extraction by hydrothermal fluids, producing abundant fluid-borne metals that are crucial for high-temperature sulfide mineralization (i.e. isocubanite). The metal contents of pyrite II are lower than those of isocubanite, as serpentinization reaction rates would have decreased with the cooling of the gabbroic intrusions, with less metal extraction occurring where pyrite II is precipitated.

However, the coexistence of hematite and magnetite in serpentine minerals of the Tianzuo hydrothermal field indicates relatively oxidizing conditions during serpentinization reactions (Fig. 4f-h). Previous studies have shown that the isocubanite has homogenous and higher δ<sup>34</sup>S values (+9.6 to +12.2‰) relative to late low-temperature pyrite II (-23.8 to -3.6‰), indicating the presence of abundant sulfate in the reaction zone (Ding et al., 2021). The abundant sulfates may produce an oxidizing environment, with sulfur as SO<sub>4</sub><sup>2-</sup> in the reaction zone. Hydrothermal fluids in the reaction zone do not become saturated in chalcophile elements, which are more soluble in oxidizing

environments, and fluids with high initial metal concentrations do not precipitate sulfides (Sun et al., 2004; Sun et al., 2011; Sun et al., 2013; Nadeau et al., 2010). The final mineralization of sulfides is controlled mainly by the behavior of reduced sulfur (S<sup>2-</sup>; Sun et al., 2004; Liang et al., 2009), which requires the reduction of sulfate in the oxidized source to sulfides or polysulfides during deposition. This has been attributed mainly to magnetite crystallization inducing sulfate reduction and corresponding oxygen fugacity fluctuations, through the following reactions (Vila and Sillitoe, 1991; Mao et al., 2009; Imai et al., 2007; Khashgerel et al., 2008; Liang et al., 2009; Xu et al., 2009):



The above reactions can produce low-pH hydrothermal fluids with an enhanced ability to extract chalcophile elements, but magnetite formed by the reactions can be further oxidized to hematite through reactions such as:



In Tianzuo, magnetite and hematite may grow alternately (Fig. 4f-h), buffering oxygen fugacity as the hematite–magnetite buffer with pH values near neutral. Initial hydrothermal fluids derived from the reaction zone could thus be enriched in S–3. Experimental studies have shown that hematite–magnetite redox buffer conditions are ideal for the formation of S–3, accounting for 50%–95% of dissolved sulfur (Pokrovski and Dubrovinsky, 2011). S–3 is similar to polysulfide ions such as S2–3 and S2–2 in that it forms strong complexes with Au, Cu, and other elements with similar behaviors in aqueous solution (Berndt et al., 1994; Pokrovski and Dubrovinsky, 2011). Sulfate reduction to S–3 is therefore very important in scavenging Cu, Au, and other similar elements (e.g., S, Se, Te, Zn, Pb, Bi, and Cd) from serpentine minerals into ore-forming fluids that are of critical importance for sulfide mineralization. The intergrowth of magnetite and hematite in serpentine minerals of the Tianzuo hydrothermal field suggests that the reactions forming them occurred in the field, explaining the higher contents of most chalcophile elements in isocubanite compared with late pyrite II.

## 6. Conclusions

This study investigated the trace-element compositions of high-temperature isocubanite and low-temperature pyrite II from the Tianzuo hydrothermal field using *in situ* LA-ICP-MS analysis, in order to further understand sulfide mineralization hosted in ultramafic rocks. Our major conclusions are as follows:

1. Gabbroic intrusions provided the abundant heat driving high-temperature hydrothermal circulation and also additional metals, particularly Te, Cu, Co, and In, to the hydrothermal system where isocubanite precipitated. The intrusion of gabbroic magma also promoted serpentinization reactions, improving the extraction ability of hydrothermal fluids and resulting in the enrichment of most ore-forming metals in isocubanite, including Cd, Se, Sn, Zn, Ag, Bi, Pb, Mn, and Ni.
2. Pyrite II mineralization was dominated by seawater convection, with serpentinization being controlled by reactions between seawater and ultramafic rocks. Low temperatures and low rates of serpentinization reactions prevented the extraction of metals from wall rocks, leading to low concentrations of ore-forming metals in pyrite II, other than Mo, Tl, which are significantly influenced by seawater.
3. The coexistence of hematite and magnetite in serpentine minerals indicates relatively oxidizing conditions in initial hydrothermal fluids derived from the reaction zone, which would have significantly increased initial concentrations of ore-forming metals in

hydrothermal fluids through enhancing the scavenging of Cu, Au, and similar elements from wall rocks during fluid migration.

## Declaration of Competing Interest

The authors declare that they have no known competing financial interests or personal relationships that could have appeared to influence the work reported in this paper.

## Acknowledgments

We are grateful to five anonymous reviewers, Dr. Kunfeng Qiu (Editor), and Dr. Franco Pirajno (Editor-in-Chief) for their thoughtful reviews and constructive comments. This work was financially supported by the National Key Research and Development Program of China under contract Nos. 2017YFC0306603 and 2018YFC0309902; Scientific Research Fund of the Second Institute of Oceanography, MNR (No. JB2001); the Foundation for Young Scientists of Jiangsu Province (No. BK20180511); the National Science Foundation for Young Scientists of China (Nos. 41803037 and 41806076); Key Laboratory of Ocean and Marginal Sea Geology, Chinese Academy of Sciences (No. OMG2019-07); Macao Science and Technology Development Fund (No. FDCT-002/2018/A1); China Postdoctoral Science Foundation (No. 2019M652043); and the COMRA Major Project under contract Nos. DY135-S1-1-01 and DY135-S1-1-02.

## Appendix A. Supplementary data

Supplementary data to this article can be found online at <https://doi.org/10.1016/j.oregeorev.2021.104421>.

## References

- Allen, D.E., Seyfried Jr, W.E., 2004. Serpentization and heat generation: Constraints from Lost City and Rainbow hydrothermal systems. *Geochimica et Cosmochimica Acta* 68 (6), 1347–1354.
- Auclair, G., Fouquet, Y., 1987. Distribution of selenium in high-temperature hydrothermal sulfide deposits at 13°N, East Pacific Rise. *Canadian Mineralogist* 25, 577–587.
- Baker, E.T., Chen, Y.J., Morgan, J.P., 1996. The relationship between near-axis hydrothermal cooling and the spreading rate of mid-ocean ridges. *Earth and Planetary Science Letters* 142 (1), 137–145.
- Barrie, C.T., Hannington, M.D., Bleeker, W.I., 1999. The Giant Kidd Creek Volcanic-Associated Massive Sulfide Deposit, Abitibi Subprovince, Canada. *Economic Geology* 8, 247–269.
- Belissont, R., Boiron, M.C., Luais, B., Cathelineau, M., 2014. LA-ICP-MS analysis of minor and trace elements and bulk Ge isotopes in zoned Ge-rich sphalerite from the Noailhac-Saint-Salvy deposit (France): insights into incorporation mechanisms and ore deposition process. *Geochim. Cosmochim. Acta* 126, 518–540.
- Beltenev, V.Y., Ivanov, V., Rozhdestvenskaya, I.I., Cherkashov, G.A., Stepanova, T., Shilov, V., Pertsev, A., Davydov, M., Egorov, I., Melekestseva, I., Narkevsky, E., Ignatov, V., 2007. A new hydrothermal field at 13°30' N on the Mid-Atlantic Ridge. *InterRidge News* 16, 9–10.
- Beltenev, V.Y., Rozhdestvenskaya, I.I., Nescheretov, A.V., Cherkashev, G.A., Sudarikov, S.M., Rumyantsev, A.B., Markov, V.F., Krotov, A.G., Zhirnov, E.A., 2002. New data on hydrothermal activity in the area of 12°57'N, MAR: Initial results of the R/V Professor Logatchev cruise 20. *InterRidge News* 11, 38–40.
- Berndt, M.E., Buttram, T., Earley, D., Seyfried, W.E., 1994. The stability of gold polysulfide complexes in aqueous sulfide solutions-100 °C to 150 °C and 100 bars. *Geochim. Cosmochim. Acta* 58, 587–594.
- Butler, I.B., Nesbitt, R.W., 1999. Trace element distributions in the chalcopyrite wall of a black smoker chimney: insights from laser ablation inductively-coupled plasma mass spectrometry (LA-ICP-MS). *Earth and Planetary Science Letters* 167, 335–345.
- Cannat, M., 1993. Emplacement of mantle rocks in the seafloor at mid-ocean ridges. *J. Geophys. Res.* 98 (B3), 4163–4172.
- Cannat, M., 1996. How thick is the magmatic crust at slow spreading oceanic ridges? *Journal of Geophysical Research* 101, 2847–2857. <https://doi.org/10.1029/95JB03116>.
- Cannat, M., Rommevaux-Jestin, C., Fujimoto, H., 2003. Melt supply variations to a magma-poor ultra-slow spreading ridge (Southwest Indian Ridge 61° to 69°E). *Geochemistry Geophysics Geosystems* 4 (8), 9104.
- Cannat, M., Rommevaux-Jestin, C., Sauter, D., Deplus, C., Mendel, V., 1999. Formation of the axial relief at the very slow spreading Southwest Indian Ridge (49 degrees to 69 degrees E). *Journal of Geophysical Research-Solid Earth*, 1999, 104(B10): 22825–22843.
- Cannat, M., Sauter, D., Bezios, A., Meyzen, C., Humler, E., Le Rigoleur, M., 2008. Spreading rate, spreading obliquity, and melt supply at the ultraslow spreading Southwest Indian Ridge. *Geochem. Geophys. Geosyst.* 9, Q04002. <https://doi.org/10.1029/2007GC001676>.
- Cao, H., Sun, Z.L., Liu, C.L., Jiang, X.J., He, Y.J., Huang, W., Shang, L.N., Wang, L.B., Zhang, X.L., Geng, W., Shi, M.J., Li, D.Y., 2018. The metallogenic mechanism and enlightenment of hydrothermal sulfide from the ultramafic-hosted hydrothermal systems at ultra-slow spreading ridge. *HaiyangXuebao* 40 (4), 61–75. <https://doi.org/10.3969/j.issn.0253-4193.2018.04.006> (in Chinese with English abstract).
- Charlou, J.L., Donval, J.P., Fouquet, Y., Jean-Baptiste, P., Holm, N., 2002. Geochemistry of high H<sub>2</sub> and CH<sub>4</sub> vent fluids issuing from ultramafic rocks at the Rainbow hydrothermal field (36° 14'N, MAR). *Chem. Geol.* 191 (4), 345–359.
- Charlou, J.L., Fouquet, Y., Bougault, H., Donval, J.P., Etoubleau, J., Jean, B.P., Dapoigny, A., Appriou, P., Rona, P.A., 1998. Intense CH<sub>4</sub> plumes generated by serpentization of ultramafic rocks at the intersection of the 15° 20'N fracture zone and the Mid-Atlantic Ridge. *Geochim. Cosmochim. Acta* 62 (13), 2323–2333.
- Chen, J., Tao, C.H., Liang, J., Liao, S.L., Dong, C.W., Li, H.M., Li, W., Wang, Y., Yue, X.H., He, Y.H., 2018. Newly discovered hydrothermal fields along the ultraslow-spreading Southwest Indian Ridge around 63°E. *Acta Oceanol. Sin.* 11, 61–67.
- Connally, D.P., Copley, J.T., Murton, B.J., Stansfield, K., Tyler, P.A., German, C.R., VanDover, C.L., Amon, D., Furlong, M., Grindlay, N., Hayman, N., Huehnerbach, V., Judge, M., LeBas, T., McPhail, S., Meier, A., Nakamura, K., Nye, V., Pebody, M., Pedersen, R.B., Plouviez, S., Sands, C., Searle, R.C., Stevenson, P., Taws, S., Wilcox, S., 2012. Hydrothermal vent fields and chemosynthetic biota on the world's deepest seafloor spreading centre. *Nat. Commun.* 3 <https://doi.org/10.1038/ncomms1636>.
- Cook, N.J., 1996. Mineralogy of the sulphide deposits at Sulitjelma, northern Norway. *Ore Geology Reviews* 11, 303–338.
- Cook, N.J., Chryssoulis, S.I., 1990. Concentrations of “invisible gold” in common sulfides. *Canadian Mineralogist* 1–16.
- Cook, N.J., Ciobanu, C.L., Pring, A., Skinner, W., Shimizu, M., Danyushevsky, L., Saini-Eidukat, B., Melcher, F., 2009. Trace and minor elements in sphalerite: a LA-ICPMS study. *Geochim. Cosmochim. Acta* 73, 4761–4791.
- Dekov, V.W., Garbe-Schönberg, D., Kamennov, G.D., Guéguen, B., Bayon, G., Bindl, L., Asael, D., Fouquet, Y., 2018. Redox changes in a seafloor hydrothermal system recorded in hematite-chalcopyrite-chimneys. *Chemical Geology* 483, 351–371.
- Dias, Á.S., Barriga, F., 2006. Mineralogy and geochemistry of hydrothermal sediments from the serpentinite-hosted Saldanha hydrothermal field (36°34'N; 33°26'W) at MAR. *Mar. Geol.* 225 (1–4), 157–175. <https://doi.org/10.1016/j.margeo.2005.07.013>.
- Dick, H.J.B., 1989. Abyssal peridotites, very slow spreading ridges and ocean ridge magmatism, in *Magmatism in the Ocean Basins*, edited by A. D. Saunders and M. J. Norry. *Geol. Soc. Spec. Publ.* 115, 71–105.
- Dick, H.J.B., Lin, J., Schouten, H., 2003. An ultraslow-spreading class of ocean ridge. *Nature* 426, 405–412.
- Ding, T., Ma, D.S., Lu, J.J., Zhang, R.Q., 2018a. Garnet and scheelite as indicators of multi-stage tungsten mineralization in the Huangshaping deposit, southern Hunan province, China. *Ore Geology Reviews* 94, 193–211.
- Ding, T., Ma, D.S., Lu, J.J., Zhang, R.Q., 2018b. Magnetite as an indicator of mixed sources for W-Mo-Pb-Zn mineralization in the Huangshaping polymetallic deposit, southern Hunan Province, China. *Ore Geology Reviews* 95, 65–78.
- Ding, T., Tao, C.H., Dias, A.A., Liang, J., Chen, J., Wu, B., Ma, D.S., Zhang, R.Q., Wang, J., Liao, S.L., Wang, Y., Yang, W.F., Liu, J., Li, W., Zhang, G.Y., Huang, H., 2021. Sulfur isotopic compositions of sulfides along the Southwest Indian Ridge: implications for mineralization in ultramafic rocks. *Mineralium Deposita* 56, 991–1006. <https://doi.org/10.1007/s00126-020-01025-0>.
- Douville, E., 1999. Les fluides hydrothermaux océaniques: comportement géochimique des éléments traces et des terres rares-Processus associés et modélisation thermodynamique. Thèse de Doctorat, Université de Bretagne Occidentale, Brest, France.
- Douville, E., Charlou, J.L., Oelkers, E.H., Bienvenu, P., Colon, C.F.J., Donval, J.P., Fouquet, Y., Prieur, D., Appriou, P., 2002. The rainbow vent fluids (36°14'N, MAR): the influence of ultramafic rocks and phase separation on trace metal content in Mid-Atlantic Ridge hydrothermal fluids. *Chemical Geology* 184 (1–2), 37–48.
- Fleet, M.E., 1970. Structural aspects of the marcasite-pyrite transformation. *The Canadian Mineralogist* 10 (2), 225–231.
- Fleet, M.E., MacLean, P.J., Barbier, J., 1989. Oscillatory-zoned As-bearing pyrite from strata-bound and stratiform gold deposits: An indicator of ore fluid evolution. *Economic Geology Monograph* 6, 356–362.
- Fouquet, Y., Charlou, J.L., Barriga, F., 2002. Modern seafloor hydrothermal deposits hosted in ultramafic rocks. *Geol. Soc. Am. Abstracts with Programs*, 34(6A), Paper No. 194-7.
- Gaal, G., Parkkinen, J., 1993. Early Proterozoic ophiolite-hosted copper-zinc-cobalt deposits of the Outokumpu type. In: Gaal, G., Parkkinen, J., Kirkham, R., Sinclair, W., Thorpe, R., Duke, J. (Eds.), *Mineral Deposit Modeling*. Geological Association of Canada, pp. 335–341.
- Gao, J.F., Zhou, M.F., Lightfoot, P.C., Wang, C.Y., Qi, L., Sun, M., 2013. Sulfide saturation and magma emplacement in the formation of the Permian Huangshandong Ni-Cu Sulfide Deposit, Xinjiang, Northwestern China. *Econ. Geol.* 108, 1833–1848.
- Genna, D., Gaboury, D., 2015. Deciphering the hydrothermal evolution of a VMS system by LA-ICP-MS using trace elements in pyrite: An example from the Bracemac-McLeod deposits, Abitibi, Canada, and implications for exploration. *Economic Geology* 110, 2087–2108.
- German, C.R., Klinkhammer, G.P., Rudnicki, M.D., 1996. The Rainbow Hydrothermal Plume, 36°15'N. MAR. *Geophysical Research Letters* 23 (21), 2979–2982.

- Ghaderi, M.J., Palin, M., Campbell, I.H., Sylvester, P.J., 1999. Rare earth systematic in scheelite from hydrothermal gold deposits in the Kalgoorlie-Norseman Region. *Western Australia: Economic Geology* 94, 423–438.
- Graham, U.M., Bluth, G.J., Ohmoto, H., 1988. Sulfide-sulfate chimneys on the East Pacific Rise, 11 degrees and 13 degrees N latitudes; Part I, mineralogy and paragenesis. *The Canadian Mineralogist* 26 (3), 487–504.
- Grant, H.L.J., Layton-Matthews, D., Peter, J.M., 2015. Distribution and Controls on Silver Mineralization in the Hackett River Main Zone, Nunavut, Canada: An Ag- and Pb-enriched Archean Volcanogenic Massive Sulfide Deposit. *Economic Geology* 110, 943–982.
- Grant, H.L.J., Hannington, M.D., Petersen, S., Frische, M., Fuchs, S.H., 2018. Constraints on the behavior of trace elements in the actively-forming TAG deposit, Mid-Atlantic Ridge, based on LA-ICP-MS analyses of pyrite. *Chemical Geology*. <https://doi.org/10.1016/j.chemgeo.2018.08.019>.
- Halbach, P., Blum, N., Münch, U., Plüger, W., Garbe-Schönberg, D., Zimmer, M., 1998. Formation and decay of a modern massive sulfide deposit in the Indian Ocean. *Mineralium Deposita* 33, 302–309.
- Hannington, M.D., 2014. Volcanogenic massive sulfide deposits. In: Holland, H.D., Turekian, K.K. (Eds.), *Treatise on Geochemistry*, Second ed. Elsevier, Oxford, pp. 463–488.
- Hannington, M.D., Bleeker, W., Kjarsgaard, I., 1999a. Sulfide mineralogy, geochemistry, and ore genesis of the Kidd Creek Deposit: Part I. North, Central, and South orebodies. *Economic Geology Monograph* 10, 163–224.
- Hannington, M.D., Bleeker, W., Kjarsgaard, I., 1999b. Sulfide mineralogy, geochemistry, and ore genesis of the Kidd Creek Deposit: Part II. The Bornite Zone. *Economic Geology Monograph* 10, 225–266.
- Hannington, M.D., de Ronde, C.D., Petersen, S., 2005. Sea-floor tectonics and submarine hydrothermal systems. In: Hedenquist, J.W., Thompson, J.F.H., Goldfarb, R.J., Richards, J.P. (Eds.), *Economic Geology 100th Anniversary Volume*. Society of Economic Geologists, Littleton, Colorado, USA, pp. 111–141.
- Heinrich, C.A., 1990. The chemistry of hydrothermal tin (-tungsten) ore deposition. *Economic Geology* 85, 457–481.
- Heinrich, C.A., Eadington, P.J., 1986. Thermodynamic predictions of the hydrothermal chemistry of arsenic, and their significance for the paragenetic sequence of some cassiteritearsenopyrite-base metal sulfide deposits. *Economic Geology* 81, 511–529.
- Herzig, P.M., Hannington, M.D., Arribas, A., 1998. Sulfur isotopic composition of hydrothermal precipitates from the Lau back-arc: Implications for magmatic contributions to seafloor hydrothermal systems. *Mineralium Deposita* 33, 226–237.
- Horner-Johnson, B.C., Gordon, R.G., Cowles, S.M., Argus, D.F., 2005. The angular velocity of Nubia relative to Somalia and the location of the Nubia-Somalia-Antarctica triple junction. *Geophys. J. Int.* 162 (1), 221–238.
- Hou, K.J., Li, Y.H., Ye, T.R., 2009. In-situ U-Pb zircon dating laser ablation-multi iron counting-ICP-MS. *Mineral Deposits* 28, 481–492 (in Chinese with English abstract).
- Houghton, J.L., Shanks III, W.C., Seyfried, W.E. Jr., 2004. Massive sulfide deposition and trace element remobilization in the Middle Valley sediment-hosted hydrothermal system, northern Juan de Fuca Ridge. *Geochimica et Cosmochimica Acta* 68, 2863–2873.
- Huston, D.L., Sie, S.-H., Suter, G.F., Cooke, D.R., 1995. Trace Elements in Sulfide Minerals from Eastern Australian Volcanic-Hosted Massive Sulfide Deposits: Part I. Proton Microprobe Analyses of Pyrite, Chalcopyrite, and Sphalerite, and Part II. Selenium Levels in Pyrite: Comparison with 634S Values and Implications for the Source of Sulfur in Volcanogenic Hydrothermal Systems. *Economic Geology* 90, 1167–1196.
- Idefonse, B., Blackman, D.K., John, B.E., Ohara, Y., Miller, D.J., Macleod, C.J., 2007. Oceanic core complexes and crustal accretion at slow-spreading ridges. *Geology* 35 (7), 623–626.
- Inai, A., Shinomiy, J., Soe, M.T., Setijadji, L.D., Watanabe, K., Warmada, I.W., 2007. Porphyry-type mineralization at Selogiri area, Wonogiri regency, Central Java. *Indonesia. Resour. Geol.* 57, 230–240.
- Janecky, D.R., Seyfried, W.E., 1984. Formation of massive sulfide deposits on oceanic ridge crust: incremental reaction models for mixing between hydrothermal solutions and seawater. *Geochim. Cosmochim. Acta* 48, 2723–2738.
- Jean-Baptiste, P., Charlou, J.L., Stievenard, M., Donval, J.P., Bougault, H., Mevel, C., 1991. Helium and methane measurements in hydrothermal fluids from the Mid-Atlantic Ridge; the Snake Pit site at 23° N. *Earth Planet. Sci. Lett.* 106 (1–4), 17–28.
- Kinsey, J., German, C.R., 2013. Sustained volcanically-hosted venting at ultraslow ridges: Piccard Hydrothermal Field. *Mid-Cayman Rise, Earth and Planetary Science Letters* 380, 162–168.
- Keith, M., Häckel, F., Haase, K.M., Schwarz-Schampera, U., Klemd, R., 2016. Trace element systematics of pyrite from submarine hydrothermal vents. *Ore Geol. Rev.* 72, 728–745.
- Kelley, D.S., Karson, J.A., Blackman, D., Fruh-Green, G.L., Butterfield, D., Lilley, M.D., Olson, E.J., Schrenk, M.O., Roe, K.K., Lebon, G.T., 2001. An off-axis hydrothermal vent field near the Mid-Atlantic Ridge at 30°N. *Nature* 412, 145–149. <https://doi.org/10.1038/35084000>.
- Khashgarel, B.E., Kavalieris, I., Hayashi, K., 2008. Mineralogy, textures, and whole-rock geochemistry of advanced argillic alteration: Hugo Dummett porphyry Cu–Au deposit, Oyu Tolgoi mineral district, Mongolia. *Mineral. Deposita* 43, 913–932.
- Koski, R.A., Clague, D.A., Oudin, E., 1984. Mineralogy and chemistry of massive sulfide deposits from the Juan de Fuca Ridge. *Geological Society of America Bulletin* 95 (8), 930–945.
- Krasnov, S.G., Cherkashev, G., Stepanova, T.V., Batuev, B.N., Krotov, A.G., Malin, B.V., Maslov, M.N., Markov, V.F., Poroshina, I., Samovarov, M.S., Ashadze, A.M., Lazareva, L.I., 1995. Detailed studies of hydrothermal fields in the Atlantic. In: Parson, L.M., Walker, C.L., Dixon, D.R. (Eds.), *Hydrothermal vents and processes*, 87. Geological Society Special Publication, London, pp. 43–64.
- Large, R.R., 1992. Australian volcanic-hosted massive sulfide deposits: Features, styles, and genetic models. *Economic Geology* 87, 471–510.
- Lein, A.Y., Ulyanova, N.V., Ulyanov, A.A., Cherkashev, G.A., Stepanova, T.V., 2001. Mineralogy and geochemistry of sulfide ores in ocean-floor hydrothermal fields associated with serpentinite protrusions. *Russian Journal of Earth Sciences* 3 (5), 371–393.
- Li, X., Maslennikov, V.V., Lein, A.Y., Ulyanov, A.A., 2012. Associations of trace elements in the sulfides of black smokers from the Broken Spur, Menez Gwen, and Snake Pit hydrothermal fields. *Moscow University Geology Bulletin* 67, 8–17.
- Liang, H.Y., Sun, W.D., Su, W.C., Zartman, R.E., 2009. Porphyry copper-gold mineralization at Yulong, China, promoted by decreasing redox potential during magnetite alteration. *Econ. Geol.* 104, 587–596.
- Liao, S.L., Tao, C.H., Li, H.M., Barriga, F.J.A.S., Liang, J., Yang, W.F., Yu, J.Y., Zhu, G.W., 2018. Bulk geochemistry, sulfur isotope characteristics of the Yuhuang-1 hydrothermal field on the ultraslow-spreading Southwest Indian Ridge. *Ore Geology Reviews* 96, 13–27.
- Liu, Y.S., Hu, Z.C., Gao, S., Gunther, D., Xu, J., Gao, C.G., Chen, H.H., 2008. In situ analysis of major and trace elements of anhydrous minerals by LA-ICP-MS without applying an internal standard. *Chem. Geol.* 257, 34–43.
- Loukola-Ruskeeniemi, K., 1999. Origin of black shales at the serpentinite-associated Cu-Zn-Co ores at Outokumpu, Finland. *Econ. Geol.* 94, 1007–1028.
- Lowell, R.P., Rona, P.A., 2002. Seafloor hydrothermal systems driven by the serpentinization of peridotite. *Geophysical Research Letters* 29 (11(26)), 1–4.
- Lusk, J., Bray, D.M., 2002. Phase relations and the electrochemical determination of sulfur fugacity for selected reactions in the Cu–Fe–S and Fe–S systems at 1 bar and temperatures between 185 and 460 °C. *Chemical Geology* 192 (3–4), 227–248.
- Mao, G.Z., R.M., H, Gao, J.F., Li, W.Q., Zhao, K.D., Long, G.M., Lu, H.J., 2009. Existing forms of REE in gold-bearing pyrite of the Jinshan gold deposit, Jiangxi province. *China. J. Rare Earths* 27 (6), 1079–1087.
- Maslennikov, V.V., Maslennikova, S.P., Large, R.R., Danyushevsky, L.V., 2009. Study of trace element zonation in vent chimneys from the Silurian Yaman-Kasy Volcanic-Hosted Massive Sulfide Deposit (Southern Urals, Russia) using Laser Ablation-Inductively Coupled Plasma Mass Spectrometry (LA-ICP-MS). *Econ. Geol.* 114, 1111–1141.
- Maslennikov, V.V., Maslennikova, S.P., Large, R.R., Danyushevsky, L., Herrington, R.J., Ayupova, N.R., Zaykov, V.V., Lein, A.Y., Tselyuk, A.S., Melekestseva, I.Y., Tessala, S.G., 2017. Chimneys in Paleozoic massive sulfide mounds of the Urals VMS deposits: Mineral and trace element comparison with modern black, grey, white, and clear smokers. *Ore Geology Reviews* 85, 64–106.
- Melchert, B., Devey, Colin W., German, C.R., Lackschewitz, Klas, Seifert, R., Walter, M., Mertens, C., Yoerger, D.R., Baker, E.T., Paulick, H., Nakamura, K., 2008. First evidence for high-temperature off-axis venting of deep crustal/mantle heat: the Nibelungen hydrothermal field, southern Mid-Atlantic Ridge. *Earth and Planetary Science Letters* 275, 61–69. <https://doi.org/10.1016/j.epsl.2008.08.010>.
- Melekestseva, I.Y., Maslennikov, V.Y., Tret'yakov, G.A., Nimis, P., Beltenev, V.E., Rozhdestvenskaya, I.I., Maslennikova, S.P., Belogub, E.V., Danyushevsky, L.V., Large, R.R., Yuminov, A.M., Sadykov, S.A., 2017. Gold- and Silver-Rich Massive Sulfides from the Semenov-2 Hydrothermal Field, 13°31'13"N, Mid-Atlantic Ridge: A Case of Magmatic Contribution? *Economic Geology* 112, 741–773.
- Melekestseva, I.Y., Tret'yakov, G.A., Nimis, P., Yuminov, A.M., Maslennikov, Y.V., Maslennikova, S.P., Kotlyarov, V.A., Beltenev, V.E., Danyushevsky, L.V., Large, R., 2014. Barite-rich massive sulfides from the Semenov-1 hydrothermal field (Mid-Atlantic Ridge, 13°30'07"N): Evidence for phase separation and magmatic input. *Marine Geology* 349, 37–54.
- Meng, Y.M., Hu, R.Z., Huang, X.W., Gao, J.F., Saserville, C., 2019. The origin of the carbonate-hosted Huize Zn–Pb–Ag deposit, Yunnan province, SW China: constraints from the trace element and sulfur isotopic compositions of pyrite. *Mineralogy and Petrology* 113, 369–391.
- Münch, U., Lalou, C., Halbach, P., Fujimoto, H., 2001. Relict hydrothermal events along the super-slow Southwest Indian spreading ridge near 63°56'E-mineralogy, chemistry and chronology of sulfide samples. *Chemical Geology* 177 (3–4), 341–349.
- Nadeau, O., Williams-Jones, A.E., Stix, J., 2010. Sulphide magma as a source of metals in arc-related magmatic hydrothermal ore fluids. *Nature Geoscience* 3, 501–505.
- Nayak, B., Halbach, P., Pracejus, B., Münch, U., 2014. Massive sulfides of Mount Jourdan along the super-slow spreading Southwest Indian Ridge and their genesis. *Ore Geology Reviews* 63, 115–128.
- Pedersen, R.B., Rapp, H.T., Thorseth, I.H., Lilley, M.D., Barriga, F.J.A.S., Baumberger, T., Fleisland, K., Fonseca, R., Früh-Green, G.L., Jorgensen, S.L., 2010. Discovery of a black smoker vent field and vent fauna at the Arctic Mid-Ocean Ridge. *Nature Communication*. <https://doi.org/10.1038/ncomms1124>.
- Pokrovski, G.S., Borisova, A.Y., Harrichou, J.C., 2008. The effect of sulfur on vapor-liquid fractionation of metals in hydrothermal systems. *Earth Planet. Sci. Lett.* 266, 345–362.
- Pokrovski, G.S., Dubrovinsky, L.S., 2011. The  $S_3^-$  ion is stable in geological fluids at elevated temperatures and pressures. *Science* 331, 1052–1054.
- Ranero, C.R., Reston, T.J., 1999. Detachment faulting at ocean core complexes. *Geology* 27 (11), 983–986.
- Revan, M.K., Genç, Y., Maslennikov, V.V., Maslennikova, S.P., Large, R.R., Danyushevsky, L.V., 2014. Mineralogy and trace-element geochemistry of sulfide minerals in hydrothermal chimneys from the Upper-Cretaceous VMS deposits of the eastern Pontide orogenic belt (NE Turkey). *Ore Geol. Rev.* 63, 129–149.
- Sato, T., Okino, K., Sato, H., Mizuno, M., Hanyu, T., Seama, N., 2013. Magmatic activities on the Southwest Indian Ridge between 35°E and 40°E, the closest segment to the Marion hotspot. *Geochemistry Geophysics Geosystems* 14 (12), 5286–5307.
- Sauter, D., Cannat, M., Meyzen, C., Bezos, A., Patriat, P., Humler, E., Debayle, E., 2009. Propagation of a melting anomaly along the ultraslow Southwest Indian Ridge

- between 46°E and 52°20'E: Interaction with the Crozet hotspot? *Geophys. J. Int.* 179 (2), 687–699. <https://doi.org/10.1111/j.1365-246X.2009.04308.x>.
- Sauter, D., Cannat, M., Rouméjon, S., Andreani, M., Briot, D., Bronner, A., Brunelli, D., Carlut, J., Delacour, A., Guyader, V., Macleod, C.J., Manatschal, G., Mendel, V., Ménez, B., Pasini, V., Ruellan, E., Searle, R., 2013. Continuous exhumation of mantle-derived rocks at the Southwest Indian Ridge for 11 million years. *Nature Geoscience* 6 (4), 314–320.
- Sauter, D., Carton, H., Mendel, V., Munsch, M., Rommevaux-Jestin, C., Schott, J.J., Whitechurch, H., 2004. Ridge segmentation and the magnetic structure of the Southwest Indian Ridge (at 50°30'E, 55°30'E and 66°20'E): Implications for magmatic processes at ultraslow-spreading centers. *Geochim. Geophys. Geosyst.* 5, Q05K08. <https://doi.org/10.1029/2003GC000581>.
- Sauter, D., Patriat, P., Rommevaux-Jestin, C., Cannat, M., Briais, A., Party, Gallieni Shipboard Scientific, 2001. The Southwest Indian Ridge between 49°15'E and 57°E: Focused accretion and magma redistribution. *Earth Planet. Sci. Lett.* 192 (3), 303–317.
- Schmidt, K., Koschinsky, A., Garbe-Schönberg, D., de Carvalho, L.M., Seifert, R., 2007. Geochemistry of hydrothermal fluids from the ultramafic-hosted Logatchev hydrothermal field, 15°N on the Mid-Atlantic Ridge: Temporal and spatial investigation. *Chemical geology* 242 (1), 1–21.
- Seal II, R.R., 2006. Sulfur isotope geochemistry of sulfide minerals. *Reviews in Mineralogy & Geochemistry* 61, 633–677.
- Seyfried Jr., W.E., Ding, K., 1993. The effect of redox on the relative solubilities of copper and iron in Cl-bearing aqueous fluids at elevated temperatures and pressures: an experimental study with application to seafloor hydrothermal systems. *Geochim. Cosmochim. Acta* 57, 1905–1917.
- Seyfried Jr., W.E., Ding, K., 1995. Phase equilibria in seafloor hydrothermal systems: a review of the role of redox, temperature, pH and dissolved Cl on the chemistry of hot spring fluids at mid-ocean ridges. *Geophys. Monogr.* 91, 248–272.
- Shanks, W.C.I.I., 2001. Stable isotopes in seafloor hydrothermal systems. *Rev. Mineralogy Geochem.* 43, 469–525.
- Shannon, R.D., 1976. Revised effective ionic radii and systematic studies of interatomic distances in halides and chalcogenides. *Acta Crystallogr A* 32, 751–767.
- Standish, J.J., Sims, K.W.W., 2010. Young off-axis volcanism along the ultraslow spreading Southwest Indian Ridge. *Nature Geoscience* 3, 286–292.
- Sun, W.D., Arculus, R.J., Kamenetsky, V.S., Binns, R.A., 2004. Release of gold-bearing fluids in convergent margin magmas prompted by magnetite crystallization. *Nature* 431, 975–978.
- Sun, W.D., Liang, H.Y., Ling, M.X., Zhan, M.Z., Ding, X., Zhang, H., Yang, X.Y., Li, Y.L., Ireland, T.R., Wei, Q.R., Fan, W.M., 2013. The link between reduced porphyry copper deposits and oxidized magmas. *Geochimica et Cosmochimica Acta* 103, 263–275.
- Sun, W.D., Zhang, H., Ling, M.X., Ding, X., Chung, S.L., Zhou, J.B., Yang, X.Y., Fan, W.M., 2011. The genetic association of adakites and Cu-Au ore deposits. *Int. Geol. Rev.* 53, 691–703.
- Tao, C.H., Li, H., Jin, X., Zhou, J., Wu, T., He, Y., Deng, X., Gu, C., Zhang, G., Liu, W., 2014. Seafloor hydrothermal activity and polymetallic sulfide exploration on the southwest Indian ridge. *Chinese Science Bulletin* 59 (19), 2266–2276.
- Tao, C.H., Lin, J., Guo, S.Q., Chen, Y.S.J., Wu, G.H., Han, X.Q., German, C.R., Yoerger, D.R., Zhou, N., Li, H.M., Su, X., Zhu, J., 2012. First active hydrothermal vents on an ultraslow-spreading center: Southwest Indian Ridge. *Geology* 40 (1), 47–50.
- Vila, T., Sillitoe, R.H., 1991. Gold-rich porphyry systems in the Maricunga Belt, Northern Chile. *Econ. Geol. Bull. Soc. Econ. Geol.* 86, 1238–1260.
- Von Damm, K.L., 1990. Seafloor hydrothermal activity black smoker chemistry and chimneys. *Annu. Rev. Earth Planet. Sci.* Lett. 18, 173–204.
- Wang, Y.J., 2012. Comparison study of mineralization of Kairei and Edmond active hydrothermal fields in Central Indian Ridge. Doctoral dissertation. 129 pp. Zhejiang University, China. (In Chinese with English abstract).
- Wetzel, L.R., Shock, E.L., 2000. Distinguishing ultramafic-from basalt-hosted submarine hydrothermal systems by comparing calculated vent fluid compositions. *Journal of Geophysical Research: Solid Earth* 105 (B4), 8319–8340.
- Wittmann, A., 1974. Indium. 49-A Crystal chemistry, in Wedepohl, K.H., ed., *Handbook of geochemistry*: Berlin, Springer-Verlag, V. II/4, 49-A-1-49-A-8.
- Wohlgemuth-Ueberwasser, C.C., Viljoen, F., Petersen, S., Vorster, C., 2015. Distribution and solubility limits of trace elements in hydrothermal black smoker sulfides: An in situ LA-ICP-MS study. *Geochim. Cosmochim. Acta* 159, 16–41.
- Wuensch, B.J., 1976. Sulfide crystal chemistry. *Reviews in Mineralogy* 1, W-21-W-44.
- Xie, L.W., Zhang, Y.B., Zhang, H.H., Sun, J.F., Wu, F.y., 2008. In situ simultaneous determination of trace elements, U-Pb and Lu-Hf isotopes in zircon and baddeleyite. *Chinese Science Bulletin* 53, 1565–1573.
- Xu, W.Y., Pan, F.C., Qu, X.M., Hou, Z.Q., Yang, Z.S., Chen, W.S., Yang, D., Cui, Y.H., 2009. Xiongecun, Tibet: a telescoped system of veinlet-disseminated Cu (Au) mineralization and late vein-style Au (Ag)-polymetallic mineralization in a continental collision zone. *Ore Geol. Rev.* 36, 174–193.
- Yamamoto, M., Kase, K., Tsutsumi, M., 1984. Fractionation of sulfur isotopes and selenium between coexisting sulfide minerals from the Besshi deposit, Central Shikoku, Japan. *Mineralium Deposita* 19, 237–242.
- Yang, A.Y., Zhao, T.P., Zhou, M.F., Deng, X.G., 2017a. Isotopically enriched N-MORB: A new geochemical signature of off-axis plume-ridge interaction-A case study at 50°28'0"E, Southwest Indian Ridge. *Journal of Geophysical Research: Solid earth* 122, 191–213.
- Yang, W.F., Tao, C.H., Li, H.M., Liang, J., Liao, S.L., Long, J.P., Ma, Z.B., Wang, L.S., 2017b.  $^{230}\text{Th}/^{238}\text{U}$  dating of hydrothermal sulfides from Duanqiao hydrothermal field, Southwest Indian Ridge. *Marine Geophysical Research* 38, 1–13.
- Yuan, B., Yu, H.J., Yang, Y.M., Zhao, Y.X., Yang, J.C., Xu, Y., Lin, Z., 2018. Zone refinement related to the mineralization process as evidenced by mineralogy and element geochemistry in a chimney fragment from the Southwest Indian Ridge at 49.6°E. *Chemical Geology* 482, 46–60.
- Zhang, T., Lin, J., Gao, J.Y., 2013. Magmatism and tectonic processes in Area A hydrothermal vent on the Southwest Indian Ridge. *Sci. China-Earth Sci.* 56 (12), 2186–2197. <https://doi.org/10.1007/s11430-013-4630-5>.
- Zhou, H.Y., Dick, H.J.B., 2013. Thin crust as evidence for depleted mantle supporting the Marion Rise. *Nature* 494 (7436), 195–200. <https://doi.org/10.1038/nature11842>.